FGF overactivation underlies reduced neurogenesis in cerebellar organoid models of neurodevelopmental ciliopathy

Ludovica Brunetti[1,2,*], Antonia Wiegering[1,2], Isabelle Anselme[1,2], Lidia Pollara[3,4], Martin Catala[1,2], Christophe Antoniewski[2], Enza Maria Valente[3,4], Sylvie Schneider-Maunoury[1,2,#,*], Christine Vesque[1,2,#,*]

1. Sorbonne Université, CNRS, Inserm, Development, Adaptation and Aging, Dev2A, F-75005 Paris, France
2. Sorbonne Université, CNRS, Inserm, Institut de Biologie Paris Seine, IBPS, F-75005 Paris, France
3. Department of Molecular Medicine, University of Pavia, Pavia, Italy
4. Neurogenetics Research Center, IRCCS Mondino Foundation, Pavia, Italy

# These authors jointly supervised this work

* co-corresponding authors

ABSTRACT

A hallmark feature of neurodevelopmental ciliopathies is the hypo-dysplasia of the cerebellar vermis, as observed among most Joubert Syndrome patients. Despite significant advances in mouse models, the pathogenetic mechanisms linking ciliary gene dysfunction to Joubert syndrome neurodevelopmental defects are still poorly understood. In this study, we generated cerebellar organoids from human induced pluripotent stem cells carrying null mutations or patient-derived variants in the Joubert syndrome causal gene *RPGRIP1L*, which encodes a scaffold protein crucial for cilia function. Using immunolabelling and transcriptomics, we show that WT organoids recapitulate early steps of cerebellar development, including the expression of markers for both Granule and Purkinje cell lineages. In contrast, cerebellar organoids derived from all *RPGRIP1L*-deficient lines exhibit a common severe reduction of Purkinje lineage markers, along with decreased neurogenesis. The neurogenesis defect is coupled to increased progenitor proliferation, as well as extended overactivation of the FGF pathway. Restoring normal levels of FGF signaling in *RPGRIP1L*-deficient organoids rescues the proliferative/neurogenic balance as well as Purkinje lineage formation. Thus, our results uncover an early FGF deregulation that hampers correct neuronal differentiation and could participate in the cerebellar phenotype of patients suffering from neurodevelopmental ciliopathies.

INTRODUCTION

Cerebellar dysfunction is a common feature of several developmental disorders, associated with both motor disease and cognitive impairment [1]. The cerebellum is a morphologically complex organ which originates from dorsal hindbrain rhombomere 1 (r1), under the influence of inductive signals emanating from the isthmic organizer (IsO) located at the midbrain-hindbrain boundary (MHB) [2]. The interface between anteriorly located *OTX2*-expressing tissue and posteriorly located *GBX2*-expressing tissue defines the position of the IsO, where fibroblast growth factor-8 (*FGF8*) expression is activated [3]. *FGF8* plays a pivotal role in the establishment of the early cerebellar territory [4,5].

Once the cerebellar territory is established, two spatially distinct germinal zones arise: the ventricular zone (VZ) and the rhombic lip (RL). The VZ gives rise to all the cerebellar inhibitory GABAergic neurons, among which the Purkinje Cells (PCs) [6], while the RL generates all the progenitors of the excitatory glutamatergic neurons, including the Granule Neurons (GNs) [7,8]. Purkinje neurogenesis in the VZ terminates early during embryo development, between post-conception weeks (PCW) 8 and 10 in humans [9,10] and embryonic days (E) 10-13 in mice [11,12]. In contrast, the production and amplification of Granule Cell Progenitors (GCPs) to generate the final pool of GNs is a longer process, with a peak of massive proliferation around 26 PCW in humans [13], and at early post-natal stages (P1-P7) in mouse [2,12]. The proliferation, maturation and migration in different directions of all the cerebellar cell types, will determine the correct aspect and functional organization of the mature cerebellar cortex [12].

Joubert syndrome (JBTS) is a rare neurodevelopmental ciliopathy affecting the cerebellum and brainstem, primarily characterized by hypoplasia/dysplasia of the medial cerebellar structure called the vermis. All JBTS patients share the so-called “molar tooth sign” (MTS) on axial brain imaging, resulting from specific cerebellar and brainstem malformations [14,15]. Clinically, JBTS manifests with various neurological symptoms, such as developmental delay, abnormal ocular movements, ataxia, and intellectual disability [16]. More than 40 causal genes have been identified, all encoding proteins involved in cilia biology [15,17]. Primary cilia are microtubular sensory organelles protruding from the surface of almost all vertebrate cells, acting as signaling hubs [18–20]. To ensure proper signaling, primary cilia composition is strictly controlled by the Transition Zone (TZ). This specific region of the cilium is composed of multiple protein

complexes that control the ciliary trafficking of various molecules, such as receptors and pathway effectors [21,22]. Among them, the JBTS-associated gene *RPGRIP1L* encodes a central scaffolding protein, essential for TZ assembly [23,24] and proper Hedgehog (HH) signaling [25,26].

Being implicated in the transduction of several signaling pathways essential during development and homeostasis, such as HH, WNT and PDGFa, primary cilia play an essential role in central nervous system (CNS) formation [19]. Pioneer studies have shown that cilia depletion by conditional inactivation of *Ift88* or *Kif3a* genes in the mouse CNS results in severe cerebellar hypoplasia and foliation abnormalities caused by a failure of Shh-dependent GCP pool expansion [27,28]. Similarly, the analysis of human JBTS fetal samples revealed a reduction of GCP proliferation associated with a lower expression of HH targets, with no difference between hemispheres and vermis [29]. This alteration may provide a molecular explanation for whole cerebellum hypoplasia but leaves unanswered the origin of the specific cerebellar vermis hypoplasia observed in JBTS patients' cerebella. Ciliogenesis is finely tuned over the course of GCP production, migration and differentiation so that the window of responsiveness to SHH ligand and other cues is tightly constrained in time and space [30–32]. Overall, the pathogenetic mechanisms linking cilia dysfunction to JBTS neurodevelopmental defects remain largely unknown and may be of diverse origins.

Indeed, mouse mutants for different JBTS-associated genes, such as *Rpgrip1l* [33], *Ahi1* [34], *Tmem67* [35], *Jbts17 (CPLANE1)* [36], *Talpid3* [37], *Arl13b* [38], present high variability in the extent of cerebellar impairment, as well as divergent underlying mechanisms and ciliary defects. For example, *Ahi1* mutant embryos present a reduction of canonical WNT activity that reduces proliferation on the cerebellar dorsal midline [34], while *Tmem67* mutant embryos display an overactivated canonical WNT pathway and reduced SHH signaling [35], suggesting that different pathogenic mechanisms may underlie JBTS in humans. Furthermore, none of these JBTS murine models faithfully recapitulate the specific cerebellar phenotype observed in JBTS patients, underscored by MTS on axial brain imaging.

In order to model early cerebellum development in humans under physiological and pathological conditions, we adopted a cerebellar organoid approach. We compared the differentiation potential of a JBTS patient-derived hiPSC line, carrying biallelic mutations in the

RPGRIP1L ciliary gene, with two *RPGRIP1L* knock-out (KO) hiPSCs lines and their isogenic WT controls. We revealed common early and severe defects in both JBTS patient-derived and *RPGRIP1L* KO cerebellar organoids. All *RPGRIP1L*-deficient organoids presented ciliary defects, morphological alterations and size increase. Most importantly, we revealed an early and aberrant up-regulation of FGF signaling upon *RPGRIP1L* impairment, resulting in increased proliferation of early neural progenitors and decreased neurogenesis. These defects were fully rescued by blocking FGF signaling after MHB induction. With this study, we uncover a causal link between the deregulation of the FGF pathway and cerebellar neurogenesis/PC production defects in a human model of neurodevelopmental ciliopathy.

RESULTS

Cerebellar organoids generated from human induced pluripotent stem cells recapitulate early steps of cerebellar development

To unravel molecular mechanisms and biological processes that may be responsible for cerebellar defects in JBTS pathogenesis, we used cerebellar organoids to model early stages of human cerebellar development *in vitro*. We optimized published protocols for generating cerebellar organoids from human induced pluripotent stem cells (hiPSCs) [39,40]. To induce neural commitment, mid-hindbrain boundary establishment and tissue self-organization, embryoid bodies were sequentially treated with fibroblast growth factor 2 (FGF2), insulin, TGFß/SMAD inhibitor (SB431542), FGF19 and stromal cell-derived factor 1 (SDF1) (**Fig. 1A).** Since dynamic culture conditions have been shown to favor faster cerebellar commitment [41], embryoid bodies were cultured under orbital agitation from day 7 onwards.

Immunostaining analysis on organoid cryosections showed the progressive organization and tissue layering over time. Few early-born neurons (HUC/D+) appeared as early as day 14, along with neural progenitors (SOX2+) (**Fig. 1B**). The two cell populations (HUC/D+ or SOX2+) self-organized and covered the whole organoid tissue by day 21 (**Fig. 1C**). At day 28, a clear layering became evident, with early-born neurons primarily located in deep regions of the organoid tissue, adjacent to an outer layer of neural progenitors, organized either at the organoid periphery or into small internal rosettes (**Fig. 1D**).

To assess the time-course of cerebellar cell type production in our experimental settings, we performed bulk RNAseq analysis on cerebellar organoids derived from two independent wild-type (WT) hiPSC lines with different genetic backgrounds, PCIi033-A (Ph2) and UCSFi001-A (Wtc11) at six timepoints of the differentiation protocol (day 0, 7, 14, 21, 28, 35). First, we validated that the organoids faithfully recapitulated the earliest stages of cerebellar development. At day 7, they expressed the main markers of the MHB (*FGF8, OTX2, GBX2, WNT1, PAX2, LMX1B*) **(Supplementary Fig. 1A).** The RNA levels of early GCP markers were gradually increasing over time, first appearing at day 7 for *PAX6* and *BARHL1*, and at day 14 for *ATOH1* **(Fig. 1E**). Of note, the mature GN marker, *GABRA6*, was not detected over the 35 days short-term organoid culture, consistent with its post-natal onset in humans [10] **(Supplementary Fig. 1B)**. Concerning the GABAergic lineage, the order of appearance of Purkinje cell (PC) markers reflected the *in vivo* maturation stages of this cell population, with

the progenitor marker *OLIG2* and the early post-mitotic marker *SKOR2* peaking at day 21, followed by the more mature PC marker *CALB1*, strongly expressed between day 28 and 35 **(Fig 1F)**. The GCP marker *BARHL1* and the PC marker *CALB1* segregated in separated domains within the organoid tissue, with few cells intermingled as shown on organoid sections **(Fig. 1G)**. Altogether these data provided strong evidence for self-organization of a cerebellar primordium and successful specification of the two main cerebellar lineages following the differentiation protocol.

Given the well-established role of the SHH pathway in GCP pool expansion during cerebellar development [42,28], we also examined *SHH* ligand expression. However, almost no *SHH* mRNA was detected over the first 35 days of cerebellar differentiation **(Supplementary Fig. 1C)**. Together with the absence of *GABRA6* expression, this result indicates that the 35 days differentiation protocol we used models early cerebellar developmental stages, preceding SHH endogenous expression by PCs.

RPGRIP1L KO and JBTS patient-derived cerebellar organoids present a severe reduction of Purkinje Cell markers and a milder decrease in Granule Cell Progenitor markers

To compare the differentiation process between healthy and JBTS pathological conditions, we took advantage of two independent *RPGRIP1L* KO hiPSC lines generated in the two different genetic backgrounds used for WT analysis (Ph2 and Wtc11) [43], which both produce early truncated proteins within the first coiled coil domain **(Fig. 2A)**, along with their isogenic WT control lines. We compared these cell lines to a hiPSC line derived from a severely affected JBTS patient (NG2266) carrying two pathogenic variants in the *RPGRIP1L* gene (p.Q684X/c.2304+1G>T) (Pollara et al. submitted) **(Fig. 2A)**. Both variants of this patient are predicted by VarSome to be null variants and are classified as pathogenic following the pathogenicity criterium “very strong” (PVS1) accordingly to the ACMG (American College of Medical Genetics and Genomics) standards and guidelines [44] and encode truncated proteins missing the second C2 domain and C-terminal RPGR-Interacting domain (RID) of the protein (see Methods).

We generated cerebellar organoids from both *RPGRIP1L* KO hiPSC lines (Ph2 and Wtc11) in parallel with their isogenic WT controls, and from the JBTS-derived hiPSC line (NG2266).

Using a specific antibody raised against the human RPGRIP1L RID domain, we showed the presence of RPGRIP1L protein at its subcellular localization at the ciliary TZ in WT organoids

(**Supplementary Fig. 2A**). On the contrary, the protein was completely absent from the TZ domain of both *RPGRIP1L* KO and JBTS patient-derived organoid cilia (**Supplementary Fig. 2B, C**).

Organoids were collected every seven days from day 0 to day 35 and a bulk RNAseq analysis was performed. We showed that both *RPGRIP1L* KO and JBTS patient-derived organoids expressed MHB markers at day 7, similarly to controls, showing proper isthmic organizer induction (**Supplementary Fig. 2D**). The GCP markers *ATOH1, BARHL1* and *PAX6* were expressed at levels comparable to WT controls across all *RPGRIP1L*-deficient conditions (**Fig. 2B, Supplementary Fig. 2E**). Quantitative PCR analysis confirmed these findings, though it revealed a slight decrease in *BARHL1* expression at day 35 in JBTS patient-derived organoids compared to controls and a significant increase in ATOH1 expression at day 35 in *RPGRIP1L* KO organoids compared to their WT counterparts (**Supplementary Fig. 2F**).

In contrast, transcriptome analysis revealed a severe reduction of numerous PC markers (*OLIG2, SKOR2, CALB1, FOXP2, PDE1C, ITPR1*) both in *RPGRIP1L* KO and JBTS patient-derived organoids compared to controls **(Fig. 2C, Supplementary Fig. 2G)**. Quantitative PCR analysis corroborated these results showing a significant decrease of *OLIG2, SKOR2* and *CALB1* markers in *RPGRIP1L* KO organoids derived from both hiPSC lines, and in JBTS patient-derived organoids compared to controls **(Supplementary Fig. 2H)**.

In order to strengthen these findings, we assayed protein expression of PC lineage markers (OLIG2, CALB1) and GCP markers (ATOH1, BARHL1) by quantifying the number of positive cells after immunostaining on organoid cryosections. Each marker was analyzed at the timepoint of highest expression in WT organoids, based on the RNAseq time-course, which corresponds to day 21 for OLIG2 and to day 28 for CALB1, ATOH1 and BARHL1. OLIG2- and CALB1-positive cells were barely detected in *RPGRIP1L* KO and JBTS patient organoids, while strong and widespread labeling was observed in WT cryosections (**Fig. 2D-E, Supplementary Fig. 3A-B, E**). Regarding the GCP lineage, the number of BARHL1 positive cells was reduced by 50% in *RPGRIP1L* KO and JBTS patient-derived organoids, along with a decrease (by 50%) in the average labeling intensity of individual cells (**Fig. 2F-G, Supplementary Fig. 3F**). The number of ATOH1 positive cells was only reduced in JBTS patient organoids (**Supplementary Fig. 3C-D)** whereas the intensity of ATOH1 labelling was reduced by ~50% both in JBTS patient and *RPGRIP1L* KO conditions (**Supplementary Fig. 3G**).

Overall, these data indicate a severe and significant impairment in the production of PCs in all *RPGRIP1L*-deficient conditions from day 21 onwards, whereas GCP specification appeared to be modestly affected, mainly at protein level from day 28.

Increased proportion of early neural progenitors in *RPGRIP1L* KO and JBTS patient cerebellar organoids

We assessed whether the molecular alterations observed upon *RPGRIP1L* impairment might be preceded by earlier defects in tissue organization. The first obvious morphological alteration under brightfield observation was a size increase of *RPGRIP1L* KO and JBTS patient organoids compared to controls, from day 21 onward **(Fig. 3A)**. Organoid area was measured every 7 days of the differentiation protocol in several independent experiments. At day 28 and 35, both *RPGRIP1L* KO and JBTS patient-derived organoids presented a significant area increase compared to WT controls (3.8-fold for *RPGRIP1L* KO and ~2.3-fold for JBTS patient organoids over WT at day 35) **(Fig. 3B)**.

Moreover, the general tissue organization was already perturbed at day 14, before overt size increase. In WT organoids, early polarized neural progenitors ($SOX2^+/ZO1^+$) formed few internal rosettes **(Fig. 3C left panels)**. In contrast, *RPGRIP1L* KO (Ph2 and Wtc11 lines) and JBTS patient-derived organoids exhibited a higher number of internal rosettes. Additionally, polarized neural progenitors (SOX2+/ZO1+) extended across the entire organoid surface, with their apical side oriented outward, creating a continuous neuroepithelium in contact with the medium **(Fig. 3C, middle and right panels)**.

Indeed, quantification of the apical marker ZO1 and the early neural progenitor marker SOX2 at day 14 showed a significant increase of the apical progenitor cell population in *RPGRIP1L* KO and JBTS patient-derived cerebellar organoids, compared to controls. The area occupied by ZO1 apical surfaces within the organoid was expanded by 4-fold in *RPGRIP1L*-KO (Ph2 and Wtc11 lines) and by 5-fold in JBTS patient organoids compared to WT condition **(Fig. 3D).** Similarly, the number of SOX2+ neural progenitors was doubled in all *RPGRIP1L*-deficient conditions compared to controls **(Fig. 3E)**

Differential dependence on RPGRIP1L protein among neural progenitors for ciliogenesis

Given the well-established role of *RPGRIP1L* in building functional cilia [23,45,24] and the fact that apical progenitors of the neural tube are ciliated [46–49], we investigated whether ciliogenesis

was affected in human cerebellar organoids. Immunostaining for the ciliary marker INPP5E and for the basal body marker gamma-TUBULIN revealed numerous cilia pointing towards the internal lumen of neural rosettes in both WT **(Fig. 4A, A')** and all *RPGRIP1L*-deficient conditions **(Fig. 4B-C'')**. Some cilia in *RPGRIP1L* KO and JBTS rosettes displayed a bulbous tip, a condition which was never observed in WT rosettes **(Fig. 4B'', C'')**. However, ciliary length was not significantly changed in *RPGRIP1L* KO rosettes and only mildly decreased in JBTS condition **(Fig. 4D)**.

We tested whether ciliogenesis was altered within non-polarized regions, as highlighted by the absence of organized nuclear orientation and the sparse distribution of gamma-TUBULIN+ basal bodies **(Fig. 4E-G)**. This analysis revealed a nearly two-fold reduction in the number of cilia in *RPGRIP1L*-KO and JBTS patient organoids on non-polarized cells (48% in *RPGRIP1L*-KO, 42% in JBTS-severe, versus 84% of mean percentage of ciliation in WT) **(Fig. 4H).** Moreover, INPP5E labeling intensity inside cilia was reduced **(Fig. 4I)** and ciliary length increased **(Fig. 4J)**. Altogether these results indicate an impaired ciliogenesis and altered ciliary trafficking in *RPGRIP1L* depleted non-polarized cells. Consistent with the literature indicating a cell type-specific requirement for *RPGRIP1L* at the ciliary transition zone (TZ) [45], our findings suggest that, in cerebellar organoids*, RPGRIP1L* is necessary for both proper ciliogenesis and ciliary content in non-polarized neural progenitors, while it appears dispensable for ciliogenesis in $ZO1^+$ early neural progenitors at day 14. Nevertheless, the observation of numerous bulbous tips on apical progenitors suggests that some of them present an abnormal content, likely to modify their signaling properties.

FGF signaling upregulation and neurogenesis impairment in *RPGRIP1L*-deficient cerebellar organoids

Bulk RNAseq datasets were analyzed to identify specific molecular pathways disrupted upon *RPGRIP1L* depletion (**Fig. 5A**). Principal Component Analysis (PCA) revealed that, at an early time point (day 7), WT, *RPGRIP1L* KO and JBTS patient samples clustered together, as shown on the PCA plot **(Fig. 5B**). At this stage, *RPGRIP1L* KO samples were closer to their isogenic WT controls than to JBTS patient replicates. However, as differentiation towards cerebellar fate progressed (e.g. day 21, day 35), *RPGRIP1L* KO samples segregated together with JBTS patient samples and formed a cluster clearly distinguishable from the WT cluster which included control samples at the same stage (**Fig. 5B**). These results provided strong evidence that

RPGRIP1L impairment similarly affected gene expression in the JBTS patient samples and *RPGRIP1L*-KO during cerebellar differentiation, regardless of the genetic background. To compare *RPGRIP1L*-KO and JBTS patient samples with the WT controls at each selected timepoint, we performed DESeq2 analysis to identify differentially expressed genes (DEGs). At day 14, many genes appeared deregulated in both *RPGRIP1L*-KO (393 genes, P value <0.001, $|\log_2 FC|>2$) and JBTS patient organoids (1058 genes, P value <0.001, $|\log_2 FC|>2$) compared to controls. The Volcano plots representing significant DEGs (P value <0.001, $|\log_2 FC|>2$) for *RPGRIP1L*-KO compared to control **(Fig. 5C**) or JBTS patient compared to control **(Fig. 5D)** highlighted many genes commonly de-regulated in both *RPGRIP1L*-deficient conditions. Most importantly, FGF signaling emerged as the first and most severely disrupted pathway, with many FGF ligands (*FGF8, FGF19, FGF17*) and direct downstream targets (*ETV4, ETV5, SPRY1-2-4*) strongly up-regulated in both *RPGRIP1L* KO and JBTS patient-derived organoids. In particular, FGF8 emerged as the top up-regulated FGF factor, with a peak of maximal over-expression at day 14 in *RPGRIP1L* KO organoids (**FC=9.45**, p value=1.79E-62) and JBTS-severe organoids (**FC=17.4**, p value=1.20E-20). Real-time quantitative PCR analysis of FGF8 expression confirmed this up-regulation between day 14 and day 21 in *RPGRIP1L*-KO and JBTS patient conditions **(Fig. 5E).**

Several *SOX* and *HES* transcription factors, important to maintain a neural progenitor state, were also significantly up-regulated in both *RPGRIP1L* KO and JBTS patient organoids. On the contrary, the neurogenic master genes, *NEUROG1*, *NEUROD1* and *NEUROD4*, were severely down-regulated as well as other genes involved in neurogenesis and early-born neuron functions likes *HES6* [50,51], *GDNF* and *RELN* (**Fig. 5C, D**). These data, summarized in the heatmap representing the log2(tpm+1) values for all the analyzed samples **(Fig. 5F),** suggest that FGF signaling upregulation in *RPGRIP1L*-deficient conditions may prevent neurogenesis by maintaining early neural cells in their progenitor state.

To better characterize the massive upregulation of FGF signaling, we assessed which cells were producing FGF8 protein. Immunostaining analysis on cryosections of day 14 organoids revealed that the strongest FGF8 signal coincided with the apical surfaces of early SOX2+/ZO1+ apical progenitors (**Supplementary Fig. 4A**). In WT organoids we could only detect signal in cells bordering the few internal lumens enriched at apical linings (**Supplementary Fig. 4B).** In *RPGRIP1L* KO and JBTS-severe organoids, FGF8 distribution was more widespread. Indeed, FGF8 was enriched on apical sides of neural progenitors forming both internal lumens

(**Supplementary Fig. 4C, D)** and the external layer covering the organoid surface (**Supplementary Fig. 4E, F)**. The overall increase of *FGF8* mRNA levels observed in *RPGRIP1L* KO and JBTS patient organoids is in line with the increased number of $SOX2^+/ZO1^+$ progenitors, identified here as the FGF8-producing cells.

***RPGRIP1L*-deficient organoids display severe neuronal maturation and extracellular matrix defects**

To assess whether the impaired neurogenesis observed at early differentiation stages (day 14) prevented the acquisition of a mature neuronal signature in *RPGRIP1L*-deficient conditions, we analyzed DEG's profile at later stages. At day 28, we observed a significant downregulation of numerous genes involved in neuronal maturation and function, both in *RPGRIP1L* KO (**Fig. 6A)** and JBTS patient **(Fig. 6B**) conditions. We also observed a severe reduction of several genes encoding extracellular-matrix (ECM) components, such as collagens and laminins, as well as integrin receptors in absence of functional RPGRIP1L protein **(Fig. 6A, B)**.

The heatmap representation of log2(tpm+1) expression values over time revealed that genes involved in axon guidance started to be up-regulated at day 21 in WT organoids, followed by genes implicated in synapse establishment at day 28. Their up-regulation was absent in both *RPGRIP1L*-deficient conditions (**Fig. 6C)**. Among these severely down-regulated genes many are known to be expressed in PCs, such as *CALB1, CBLN1* and *PCP4*.

ECM genes showed a highly dynamic expression profile over time in WT organoids with some components specifically expressed at early stages (day 14 - day 21) and others expressed at later stages (day 28 – day 35), as revealed by heatmap representation (**Supplementary Fig. 5A**). *RPGRIP1L* KO and JBTS patient organoids failed to express various ECM genes such as collagens and laminins from day 14 onwards. Plotting the log2(tpm+1) values for some deregulated components of the ECM-receptor system (*COL1A1, COL11A2, LAMA4, ITGA4*), revealed high reproducibility of the expression levels among WT samples or *RPGRIP1L*-deficient samples in four independent experiments and different genetic backgrounds (Ph2, Wtc11, NG2266 lines) (**Supplementary Fig. 5B**).

Gene ontology analyses performed to identify overrepresented gene categories in our DEG lists corroborated these results. Indeed, the most significantly enriched GO terms (- log10(p value) = 5-20) among the downregulated genes in both *RPGRIP1L* KO (**Fig 6D**) and JBTS patient (**Fig 6E**) conditions at day 21 and day 28 included neuronal differentiation (GO:0045664;

GO:0021953), axon development (GO:0061564) and axon guidance (GO:000741l), synaptic signaling (GO:0099536, GO:0099537) and synapse organization (GO:0050808), regulation of membrane potential (GO:0042391), but also core matrisome (M5884) and ECM organization (GO:0030198). Complementary "*Ensemble of Gene Set Enrichment Analyses"* (EGSEA) confirmed these results in *RPGRIP1L* KO and JBTS patient organoids for both synapse establishment and ECM organization (**Supplementary Fig. 5C**).

Altogether these results demonstrated a neuronal maturation impairment, following FGF upregulation and neurogenesis defects at early stages, and highlighted a concomitant transcriptional downregulation of major ECM components.

Blocking FGF signaling rescues neurogenesis in *RPGRIP1L*-KO cerebellar organoids

To test the hypothesis that an increased FGF signaling upon *RPGRIP1L* depletion is at the origin of neurogenesis and neuronal differentiation impairment, by maintaining neural cells in their early progenitor state, we designed a drug rescue experiment. Given that FGF8 expression is crucial for MHB formation at early stages and that, in *RPGRIP1L*-deficient organoids, the over-expression of FGF ligands and of their downstream targets started before day 14 and continued until day 21, we treated *RPGRIP1L*-deficient organoids (both KO and JBTS patient lines) with the pan-FGFR inhibitor BGJ-398 from day 11 to day 18 (**Fig. 7A**). Notably, BGJ-398 treatment restored a normal size of *RPGRIP1L*-KO and JBTS patient organoids (**Supplementary Fig. 6A, B**). Quantitative PCR analysis of *FGF8* and its downstream targets (*ETV4, ETV5, SPRY1*) revealed that BGJ-398 drug treatment completely restored the expression of these genes to WT levels at all timepoints analyzed (**Fig 7B-C'; Supplementary Fig. 6C, D**). Most importantly, expression levels of proneural genes, *NEUROG1* and *NEUROD1*, as well as PC markers, *SKOR2* and *CALB1*, were partially rescued in *RPGRIP1L* KO and JBTS patient organoids upon BGJ-398 treatment, in particular at their peak of expression (**Supplementary Fig. 6E-H**). Immunofluorescence analysis on cryosections of day 14 organoids corroborated these results showing a significant rescue in the number of positive nuclei for either NEUROD1, HUC/D or SOX2 markers, upon BGJ-398 treatment (**Fig. 7D**). Indeed, almost no NEUROD1 labeled cells or HUC/D early-born neurons could be detected in neither *RPGRIP1L* KO nor JBTS patient derived cryo-sections. The expression of both markers was totally rescued to WT levels after BGJ-398 treatment (**Fig. 7E, F**). On the other hand, the number of $SOX2^+$ cells, that was increased in all *RPGRIP1L*-deficient conditions compared to controls, was significantly reduced

by FGFR inhibition (**Fig. 7G**). The PC progenitor marker OLIG2 was also significantly rescued upon BGJ-398 treatment in both *RPGRIP1L* KO and JBTS patient-derived organoids, as shown by immunofluorescence analysis at day 21 (**Supplementary Fig. 6I-J**).

Thus, downregulating FGF signaling efficiently rescues the neurogenesis defect in *RPGRIP1L*-deficient cerebellar organoids.

Neural progenitor proliferation is increased in *RPGRIP1L*-deficient organoids and is rescued by blocking FGF signaling

To test whether the size increase observed upon *RPGRIP1L* impairment could be due to sustained proliferation caused by FGF overexpression, we assessed the proliferative potential of neural progenitors in WT, *RPGRIP1L*-KO and JBTS patient-derived organoids by carrying EdU pulse-chase experiments. We provided a 2h EdU pulse to the organoid cultures at day 18, just before the onset of size increase. Some organoids were fixed 2h after the pulse. At this stage (day 18), all *RPGRIP1L*-deficient organoids showed an increase of EdU positive cells compared to WT (1.6-fold *RPGRIP1L* KO, 2.6-fold JBTS patient). BGJ-398 treatment significantly reduced the number of EdU-incorporating cells in *RPGRIP1L* KO but not in JBTS patient organoids (**Fig. 8A, B**). Of note, similar results are obtained whether considering the number of double $EdU^+/SOX2^+$ cells among the population of $SOX2^+$ cells, indicating more progenitors in S-phase (**Fig. 8C**).

A chase assay was performed by fixing organoids five days after the EdU pulse (i.e. day 23). The number of EdU Label Retaining Cells (LRCs) was strongly reduced in both *RPGRIP1L* KO and JBTS patient conditions compared to WT (~2-fold decrease) **(Fig. 8D, E)**. This indicates that, in the time-window analyzed (between day 18 and day 23), *RPGRIP1L* KO and JBTS patient cells proliferated more than controls leading to the dilution of most EdU labeling. BGJ-398 treatment significantly restored the number of LRCs in both *RPGRIP1L* KO and JBTS patient organoids **(Fig. 8D, E)**. EdU co-labeling with the progenitor marker SOX2 and the quantification of double $EdU^+/SOX2^+$ cells among the $SOX2^+$ population showed similar results (**Fig. 8F**).

In addition, when dividing EdU+ cells into two categories—"strong" and "faint"—based on labeling intensity, we observed that the "strong" EdU+ population, likely representing cells that underwent at most one division after EdU incorporation, was the most affected in both *RPGRIP1L*-deficient conditions and restored by BGJ-398 treatment **(Fig. 8G)**. Overall, FGF overactivation in RPGRIP1L-deficient cerebellar organoids maintains SOX2+ progenitors in a

proliferative state and prevents their switch to neuronal differentiation and maturation, reducing drastically PC formation.

DISCUSSION

The crucial role of primary cilia for proper cerebellar development has been demonstrated in mouse mutants for ciliary genes, which presented varying degrees of cerebellar hypoplasia [33–38]. However, the precise mechanisms linking mutations in ciliary genes to human cerebellar impairment, as well as the developmental origin of specific JBTS patient cerebellar features, remain largely unknown. Importantly, critical aspects of this disease may be missed in mouse models, as cerebellar formation in humans presents unique features [10,13,52]. To overcome this issue, in this study we leveraged human cerebellar organoids to investigate the formation of early cerebellar progenitors under healthy and pathological conditions linked to mutations in *RPGRIP1L*, a JBTS causal gene. Our study uncovered an increased proliferation of neural progenitors and a reduction of neurogenesis in *RPGRIP1L*-deficient cerebellar organoids. These defects are correlated with a strong FGF pathway upregulation. Rescue experiments by blocking FGF receptors (FGFRs) demonstrate the causal link between FGF up-regulation and neurogenesis-proliferation imbalance.

While MHB markers were expressed at day 7 at similar levels in all genotype conditions, temporal expression analysis of typical cerebellar cell markers revealed a strong reduction of all analyzed markers of the PC lineage, from day 21 to 35. Whether this reflects a defect in PC specification and or differentiation remains to be determined. PCs being early-born neurons in the human cerebellum (8-10 PCW) [9,10], the strong defect in their production in *RPGRIP1L*-deficient organoids might be linked to the general neurogenesis defect. Indeed, the concurrent rescue of neurogenesis and expression of PC marker (OLIG2, SKOR2, CALB1) following FGFR inhibitor treatment strongly suggests that the two defects are linked. The GCP population appears less affected when considering GCP marker RNA levels. However, we did observe a 50% reduction in the number and staining intensity of BARHL1-expressing cells at day 28, suggesting that the glutamatergic lineage might also be affected at later stages, consistent with the late maturation (post-natal) of GNs in humans [10]. Transcriptome analysis

also revealed a severe downregulation of several integrins and ECM components, perturbing the ECM-receptor system in *RPGRIP1L*-deficient organoids. Although the causes of this alteration are unclear, it might participate in the neurogenesis and neuronal maturation impairment in *RPGRIP1L*-deficient organoids. Indeed, the expression of ECM molecules is dynamically regulated during brain development and plays prominent roles in neurogenesis, cell migration, neurite outgrowth and synaptogenesis [53–55].

FGF8 is known as the key morphogen to establish early cerebellar territory *in vivo* [56]. Notably, the dose, the precise location and the time window of FGF8 expression need to be tightly controlled to allow proper cerebellar development [57]. Ectopically upregulating *Fgf8* in cerebellar precursors increases their proliferation and overrides their normal program of cell specification [58]. Moreover, conditional inactivation in the mouse isthmus of more than one *Sprouty* gene (*Spry1-2-4*), which are FGF direct targets acting as feedback loop negative regulators [59], results in overactivation of FGF signaling and aberrant cerebellar development [60]. A growing body of literature emphasizes the role of the FGF pathway in regulating the proliferative/neurogenic balance in early neural development, by promoting progenitor proliferation at the expense of neuronal differentiation during embryonic spinal cord elongation [61–63] and corticogenesis [64,65]. In our cerebellar differentiation protocol, WT organoids downregulated *FGF8* after day 7, while *RPGRIP1L*-deficient organoids displayed a massive FGF8 up-regulation from day 14 to 21. Consistent with current literature, we showed that the increased levels of FGF ligands (*FGF8, FGF17, FGF19*) and pathway activation, as indicated by the expression of *ETV*4-5 target genes, were responsible for the impaired neurogenesis and neuronal differentiation observed upon *RPGRIP1L* depletion.
We identified apical neural progenitors as the FGF8 producing cells, with strong FGF8 protein accumulation at their apical pole. We further showed that this apical progenitor pool was expanded in *RPGRIP1L*-deficient conditions. Whether this expansion is the initial cause of higher FGF production or the consequence of an increased FGF signaling and sustained proliferation remains to be determined. Nevertheless, we provided evidence that, once engaged, this mechanism could be self-sustaining.

Interestingly, the development of the vermis region in mice relies on a higher and longer FGF8 dosage than the hemispheres [57,66]. Indeed, during early developmental stages, the region

closest to the FGF8-expressing territory at the IsO corresponds to the prospective vermis [67], which has been identified as a direct derivative of these FGF8-expressing isthmic cells [68]. This further underscores the importance of dissecting the role of early FGF overactivation in *RPGRIP1L*-deficient cerebellar organoids and how this could impact cerebellar development at later stages. It is tempting to speculate that hyper-proliferation and impaired neurogenesis, due to prolonged and exacerbated FGF signaling on rostral region at early stages, could result in cell death of the undifferentiated progenitors and potentially in cerebellar vermis hypoplasia at later stages. A similar phenomenon of over-proliferation followed by widespread apoptosis has been observed in chicken embryos upon loss of function of the kinase DYRK1A, and has been proposed to result from uncoupling between cell cycle exit and neuronal differentiation [69].

The JBTS patient donor of the NG2266 cell line used in this study, exhibits a very severe neurological phenotype, correlated with vermis hypoplasia and partial aplasia, as revealed by encephalic magnetic resonance imaging (MRI). The patient carries two biallelic heterozygous mutations in the *RPGRIP1L* gene: a nonsense mutation at the end of the first C2 protein domain, and a splice variant that results in the generation of a stop codon at the beginning of the second C2 domain. Given the importance of both C2 domains for RPGRIP1L function [70,71,33,72,23], a stop codon in these domains is likely to impair protein functionality. Indeed, similar to the *RPGRIP1L* KO condition, JBTS patient (NG2266)-derived organoids lacked RPGRIP1L protein at the ciliary transition zone. This further underscores the strong phenotypical similarity observed between *RPGRIP1L* KO and JBTS patient (NG2266)-derived organoids.

Given the important role of RPGRIP1L for ciliary functions, we analyzed cilia formation and ciliary content in *RPGRIP1L*-deficient cerebellar organoids compared to WT. We showed that the RPGRIP1L protein is differentially required for ciliogenesis in early neural progenitors, since its loss causes severe ciliary defects in non-polarized progenitors, while mild morphological defects are observed in polarized apical progenitors. This difference may result from variations in ciliogenesis pathways and reinforces existing literature indicating a cell type-specific requirement for RPGRIP1L at the ciliary transition zone (TZ). Indeed, studies in mice have demonstrated that in specific cell types, compensatory mechanism involving the

RPGRIP1L paralogue - RPGRIP1 - could overcome RPGRIP1L depletion [45]. Moreover, in depth analysis of cilia distribution and morphology in the mouse cerebral cortex and cerebellum challenged the traditional view that cilia are uniformly present and identical in all brain regions and cell types [73,74,32], a variability that may, at least partially, contribute to the differential vulnerability of brain regions to mutation in ciliary genes.

Reduced number of cilia on non-polarized cells could either result from decreased ciliogenesis, or increased ciliary instability/disassembly.

To date, there is no evidence in the literature supporting a direct role of primary cilia in modulating FGF signaling or indicating the presence of FGFR on the ciliary membrane. Thus, the mechanism(s) by which mutations in the JBTS-associated gene *RPGRIP1L* lead to FGF upregulation in human cerebellar organoids remain unclear. An interesting hypothesis for the initiation of FGF overexpression in *RPGRIP1L*-deficient organoids, and its link with cilia and *RPGRIP1L* protein, involves a reduction in the transcriptional repressor GLI3-R. Indeed, GLI3-R plays an important role in FGF downregulation in various systems [75–77]. Gli3R is typically produced in the absence of SHH ligands and defects in its production by proteolytic cleavage at the ciliary base are a common feature of several mouse mutants for ciliary genes , representing a potential common pathogenetic mechanism that needs to be investigated in the future.

More generally, it will be crucial to determine whether the molecular alterations reported in this study have broader relevance by also occurring in cerebellar organoids with mutations in other JBTS genes, or if they are specific to *RPGRIP1L* depletion. Indeed, not all JBTS patients present cerebellar vermis hypoplasia; in milder cases, the cerebellar vermis may be dysplastic without a reduction in size. It will be particularly helpful to investigate whether FGF signaling could be specifically disrupted in cerebellar organoids from patients with severe vermis hypoplasia, as it might be of predictive value for the severity of the neurological phenotype.

In conclusion, with this work we provide an example of a cerebellar organoid approach to investigate potential pathogenetic mechanisms underlying a human disease. Our results uncover unexpected defects in neurogenesis linked to increased FGF signaling, thereby offering a novel framework for investigating the etiology of cerebellar defects in JBTS and other neurodevelopmental diseases.

MATERIAL AND METHODS

hiPSC culture

hiPSCs were thawed in mTeSR+ medium (Stem Cell Technologies #100-0276) in the presence of Rock-inhibitor Y-27632 (5µM, Stemgent-Ozyme #04-0012) and cultured on Matrigel (Corning, VWR #354277) coated plates under standard conditions at 37°C upon confluency of 70-80%. The medium was changed every two days. Passaging was performed using ReLeSR (Stem Cell Technologies #05872) and testing for potential mycoplasma contamination was performed regularly by Eurofins genomic (Mycoplasmacheck). Accutase (Stem Cell Technologies #07920) was used for the dissociation of hiPSC colonies into single cells prior to the differentiation protocol.

Identification of the *RPGRIP1L* RNA product derived from the NG2266 hiPSC c.2304+1G>T splice variant allele.

We demonstrated by sequencing PCR products from NG2266 hiPSCs cDNA that the splice variant c.2304+1G>T resulted in intron retention leading to an early stop codon at position 788 (S788X). Primer 1 (Forward: GTATCCATAAACTAGAAGCCCAAT) was designed at the junction between exon 14 and 15; primer 2 (Reverse: GGGTTAAGGTTACAGGGGATCTC) was placed in the intron between exon 16 and 17; Primer 3 (Reverse: AATATTCCTGAGATACACCTGTC) was positioned at the junction between exon 17 and 18 **(Supplementary Fig. 7A)**. PCR products were analyzed on agarose gel and showed that primer pair 1-2 amplified an 813 bp region in the cDNA derived from JBTS patient (NG2266) hiPSCs but not from the WT condition **(Supplementary Fig. 7B)**. Primer pair 1-3 amplified a 1009 bp region, both in the WT and in JBTS patient cDNA. As expected, NG2266 second allele (c.2050C>T/p.Q684X) present a missense mutation that does not affect the cDNA structure, resulting in a PCR product of the same size as WT alleles. On the contrary, using the primer pair 1-3, the c.2304+1G>T allele could not be amplified from cDNA given that intron retention would give rise to a 3969 bp PCR product **(Supplementary Fig. 7B')**.

Primer pair 1-2 PCR product from NG2266 hiPSCs was sequenced to confirm the intron retention. An ATG stop codon appear 29 nt after the beginning of the intron sequence, most likely giving rise to a truncated form of the protein **(Supplementary Fig. 7C)**.

Moreover, an additional mutation was identified in the exon 16: c.2231 G>A (p. R744Q).

Differentiation of hiPSCs into cerebellar organoids

After two amplification passages, hiPSC lines were dissociated into single cells using Accutase (Stem Cell Technologies #07920) and resuspended in mTeSR+ medium supplemented with 10 µM ROCK inhibitor. Then, cells were promptly re-aggregated using AggreWell™800 microwell plates (StemCell Technologies) following the manufacturer's instructions. Cells were seeded at a density of 1.8 × 10^6 cells per well (6,000 cells per microwell). This corresponded to day 0 of the cerebellar differentiation protocol. Two days later the entire medium was replaced with the chemically defined medium (gfCDM), slightly modified compared to [39], consisting of vol:vol Isocove's modified Dulbecco's medium (Thermo Fisher #12440053)/Advanced DMEM/F-12 (Thermo Fisher #12634028), chemically defined lipid concentrate (1% v/v, Thermo Fisher #11905031), monothioglycerol (450 µM, Sigma #M6154), apo-transferrin (15 µg/ml, Sigma #T1147), crystallization-purified BSA (5 mg/ml, >99%, Sigma #5470), and 50 U/ml penicillin/50 µg/ml streptomycin (P/S, Thermo Fisher #15140122). The medium was also supplemented with insulin (7 µg/ml, Sigma #I9278) and used from day 2 to day 21. Different factors were added to the medium at different timepoints as represented in Fig. 1A. Recombinant human basic FGF (FGF2, 50 ng/ml, PeproTech # 100-18B) and SB431542 (SB, 10 µM, Stemgent-Ozyme #04-0010) were added to the culture on day 2. On day 4, floating aggregates were transferred from microwell plates to ultra-low attachment dishes (Corning #3261) and total medium change with drug refreshment was performed. On day 7 embryoid bodies(EBs)-containing dishes were transferred to an orbital shaker (3 mm orbit, Thermo Scientific #88881102B) and maintained under orbital agitation of 100 rpm until the end of the protocol. Total medium change with 2/3 of the initial amount of FGF2 and SB431542 was performed on day 7, day 9 and day 11. On day 14, FGF2 and SB431542 were replaced by medium change supplemented with recombinant FGF19 (100 ng/ml; PeproTech #100-32). The same medium change was also performed at day 16 and 18. From day 21 onward, the aggregates were cultured in Neurobasal medium (Thermo Fisher #21103049) supplemented with GlutaMax I (Thermo Fisher #35050061), N2 supplement (Thermo Fisher #17502048), and P/S 1% (Thermo Fisher #15140122). Total medium changes were performed on day 23, 25, 28, 30 and 32. Recombinant human SDF1 (300 ng/ml, PeproTech #300-28A) was added to the culture from day 28 onward (Fig. 1A).

EdU treatment and labeling

Cerebellar organoids at day 18 were incubated using 10 µM EdU (Click-iT EdU Imaging Kit, Invitrogen) dissolved in growth medium for 2 h at 37 °C and then washed twice with PBS. Around 30 organoids per genotype were collected and fixed for 20 minutes at room temperature in 4% cold PFA. The remaining organoids, around 30 per genotype, were kept in culture after washing for a 5-day chase until day 23 of the differentiation protocol, when they were collected and fixed in the same way.

Fixed organoids were embedded in OCT following the procedure described in the section Organoids embedding and Cryosectioning**.** EdU labeling detection on cryosections was performed according to the Click-iT EdU Imaging Kit manufacturer's instruction at the end of our immunostaining protocol (refer to the following section "Immunofluorescence").

Organoid Size Analysis

To monitor the organoid size, bright-field images were acquired at different time-points (every seven days). Organoid area was calculated by manually dragging a line with the freehand selections tool on Fiji (ImageJ; National Institutes of Health) and subsequently measuring the object area. Organoid area was measured in several independent experiments (N=3 Ph2 line, N=3 Wtc11 line, N=3 NG2266 line), at least n=10-60 organoids were analyzed per experiment per condition. Results are presented as the mean ± SEM of organoid averages from each individual experiment.

Organoids embedding and Cryosectioning

Human cerebellar organoids were collected every seven days during differentiation from day 7 to 35, rinsed with PBS and fixed in cold PFA (4 %) for 20 min at 4 °C. Then organoids were rinsed in PBS and incubated in 30 % sucrose in PBS until completely saturated. Cryoprotected organoids were embedded in OCT matrix (Cell Path #KMA-0100-00A) in plastic molds and stored at -80 °C. 12 µM cryostat sections were prepared and stored at -20 °C.

Immunofluorescence

Cryostat sections human cerebellar organoids were washed in PBS/0.1% Triton X-100. Optional steps of post-fixation with MeOH (100%) for 10 min or antigen-retrieval with Citrate-Buffer were performed depending on the antibody and specimen. After washing, cryosections

were incubated with a blocking solution containing 10% NGS in PBS/0.1% Triton-X100 for at least 2 hours. The sections were incubated overnight at 4 °C with primary antibodies (Table S1) diluted in a solution containing 1% NGS in PBS/0.1% Triton-X100. Next day, the slides were washed 3 x 10 min with PBS/0.1% Triton-X100 and incubated with secondary antibodies (Table S1) and DAPI (Merck #1.24653) diluted in 1% NGS/PBS/0.1 % Triton X-100 for 2 hours. After final washing steps with PBS/0.1 %Triton X-100 for at least 1 hour, sections were mounted with Mowiol (Roth #0713.2).

Image acquisition

Fluorescence image acquisition of cerebellar progenitors and neuronal markers was performed at room temperature using a Zeiss Observer Z1 equipped with an Apotome module, an Axiocam 506 monochrome cooled CCD camera and a 20x objective. Z-stacks with 1 µM step were acquired. All images were processed with Zen software (blue edition). For cilia analyses, fluorescence images were acquired at room temperature using a confocal microscope (LSM 980 upright, Carl Zeiss AG) and a 63x oil objective with a NA 1.4 and a monochrome charge-coupled device camera. Z-stacks with 0.25 µM step were acquired. Images were processed with Zen software (black edition).

Quantification of immunofluorescent staining and statistical analyses

The number of positive cells in immunofluorescence staining was quantified on 7µm Z-projections using the Cellpose environment (https://cellpose.readthedocs.io/en/latest/installation.html) for cell segmentation. Each image was segmented using the DAPI channel to generate a mask identifying all nuclei. The intensity of the target channel was then measured for each nucleus by uploading the MAX-projection image and the corresponding ROI mask (generated with Cellpose) into Fiji (ImageJ; National Institutes of Health). Mean intensity was calculated for each ROI, and a threshold was applied to distinguish marker-positive cells from background immunostaining. Only cells above this threshold were counted, and the ratio to the total number of nuclei (ROIs in the mask) was determined. Nuclei smaller than 20 μm^2 were excluded, as they were considered pycnotic cells.

For quantitative analyses of ZO1 staining at the apical side of the cells, positive areas were defined and measured by manually setting common thresholds in Fiji for all genotypes. For

each image, the DAPI positive area was also determined and measured by manually setting thresholds. The percentage of ZO1 positive area per organoid slice was determined after dividing the ZO1 calculated area by the DAPI area.

Analysis of ciliary density was performed by manually counting the number of cilia axonemes (INPP5E staining) over the number of basal bodies (Gamma-Tubulin staining). Measurements of axonemal INPP5E intensity and ciliary length were performed on unprocessed images (raw data) using a custom Matlab script for recognizing and measuring ROIs (cilia) properties. After quantifications were performed, representative images were processed by means of background subtraction and contrast settings via Fiji.

All data are presented as mean ± SEM. One-Way ANOVA Kruskal-Wallis and Dunn's test were performed and the following statistical significances were considered: *P<0.033, **P<0.0021, ***P<0.0002 and ****P<0.0001. All statistical data analysis and graph illustrations were performed using GraphPad Prism (GraphPad Software).

Total RNA isolation and qPCR analyses

WT, *RPGRIP1L* KO and JBTS patient-derived cerebellar organoids from different hiPSCs lines (Ph2, Wtc11, NG2266) and several independent experiments were collected every seven days from day 7 to 35 of the differentiation protocol and washed with PBS. RNA was isolated using the RNeasy Kit (Qiagen #74104) and RNAse-free DNase Set (Qiagen #79254) following manufacturer's instructions. 1µg of isolated RNA was retro-transcribed into cDNA using the GoScript Reverse Transcriptase Kit (Promega #A5001). For quantitative real-time PCR, a cDNA dilution (equal to 15 ng of starting RNA per well) was used in a Maxima SYBR Green/ROX qPCR Master Mix 2x (Thermo Scientific #K0222). Duplicate reactions for each sample were prepared and the samples were run in a Step One Real-Time PCR System Thermal Cycling Block (Applied Biosystems #4376357). GAPDH housekeeping gene was used as reference. Primer pairs are listed in Table S2. The analysis of real-time data was performed using the included StepOne Software version 2.0 and graphs were generated using GraphPad Prism (GraphPad Software).

Total RNA isolation and Bulk RNAseq analysis on cerebellar organoids

WT, *RPGRIP1L* KO and JBTS patient-derived cerebellar organoids from different hiPSCs lines (Ph2, Wtc11, NG2266) and several independent experiments were collected every seven days

from day 7 to 35 of the differentiation protocol and washed with PBS. Samples derived from Ph2 hiPSC line were collected from 3 independent experiments for the WT condition (Ph2, WT N=3 day 14-21-28-35, N=2 day 7, N=1 day 0) and from 2 independent experiments for the *RPGRIP1L* KO condition (Ph2, *RPGRIP1L* KO N=2 day 7-14-21-28-35, N=1 day 0). Samples derived from NG2266 JBTS patient hiPSC line were collected from 2 independent experiments (NG2266, JBTS patient N=2 day 7-14-21-28-35, N=1 day 0). Additional WT and *RPGRIP1L* KO samples were collected from the Wtc11 hiPSC line in one experiment (Wtc11, WT N=1 day 0-7-14-21-28-35, *RPGRIP1L* KO N=1 day 0-7-14-21-28-35).

RNA was isolated using the RNeasy Kit (Qiagen #74104) and RNAse-free DNase Set (Qiagen #79254). RNA quality was determined by measuring the RNA integrity number (RIN) via the High Sensitive RNA Screen Tape Analysis kit (Agilent Technologies #5067) on the TapeStation system (Agilent Technologies). A RIN above 9.5 was considered as good quality RNA and 250 ng RNA in a total volume of 25 µl was prepared per sample for further procedure. Bulk RNAseq was realized by the Genotyping and Sequencing Core Facility of the Paris Brain Institute (iGenSeq, ICM Paris). Poly A stranded cDNA libraries were built with the kit “Illumina® Stranded mRNA Prep” and their quality checked on “AGILENT Tapestation 2100”. 125 ng of each library was sequenced on both strands to produce between 33-44 Millions reads (100 bases long) using a Novaseq6000 ILLUMINA.

RNAseq data processing was performed in Galaxy under supervision of the ARTBio platform (IBPS, Paris). Paired-end RNA reads were aligned against the homo sapiens hg38 genome by using the STAR aligner (v2.7.10, Galaxy wrapper v4) [78] and the gene annotations gtf files GRCh38.109. Quality of sequencing was controlled with fastQC (Galaxy wrapper v0.74+galaxy0) and MultiQC (Galaxy wrapper v1.11+galaxy1) [79]. Gene expression was assessed by counting sequencing reads aligned to gene exons with featureCounts (Galaxy wrapper v2.0.3+galaxy2) [80]. Raw counts were further converted to normalized gene expression values using the log2(tpm+1) transformation where tpm is the count of transcript aligned reads per length of transcript (kb) per million of total mapped reads (Galaxy tool "cpm_tpm_rpk" v0.5.2). Principal Component Analyses (PCA) were performed using r-factominer (v.2.9, Galaxy tool id "high_dimensions_visualisation" v4.3+galaxy0) [81] and heatmap visualizations were produced with the Galaxy tool "high_dim_heatmap" (v3.1.3+galaxy0) using the normalized gene expression values. Differentially expressed genes (DEGs) were selected from the gene raw read counts using DESeq2 (Galaxy wrapper

v2.11.40.8+galaxy0) [82] and the Benjamini-Hochberg p-adjusted cutoff 0.01. DESeq2 statistical tables were used for generation of Volcano Plots (Galaxy tool id "volcanoplot" v0.0.5) [83], for the analysis of overrepresented gene ontology (GO) categories (Metascape online software, https://metascape.org/gp/index.html#/main/step1) [84], as well as for Ensemble of Gene Set Enrichment Analyses (EGSEA) (Galaxy wrapper v1.20.0).

ACKNOWLEDGEMENTS

We particularly thank Chloé Chaumeton and France Lam from the IBPS imaging platform I2PS for their help on image acquisition. We thank the IBPS Bioinformatics facility of which C.A. is a former member. We thank the iGenSeq sequencing platform at the ICM for reliable and fast processing of our samples. We are very grateful to Stéphane Nedelec for providing advice on BGJ-398 drug usage in hiPSCs. We thank Alexis Eschstruth for his kind contribution to the PCR analysis to identify the cDNA product of JBTS patient c.2304+1G>T splice variant. We are very grateful to Pierre Luc Bardet for his advice in generating custom Matlab scripts for cilia analysis. We thank Virginie Sottile for her support. This work was supported by funding to SSM from the *Fondation pour la Recherche Médicale (Equipe* FRM EQU201903007943), from the *Fondation pour la Recherche sur le Cancer* (ARCPJA2024080008603), from the *Agence Nationale de la Recherche* - ERA-NET Neuron 2021 “NDCil” (ANR-21-NEU2-0009-03) project and PRC AAPG2024 “CiCerO” project, from the *Fondation Maladies Rares* and the *Association Mieux vivre avec le syndrome de Joubert* under the reference “ASSOJoubert_2024_Schneider”. L.B.’s PhD was funded by Sorbonne Université (Doctoral school *Complexité du Vivant* ED515). A.W. received funding from the German Research Foundation (DFG; WI 5451/1-1)
Work in E.M.V.’s lab was supported by Italian Ministry of Health - ERA-NET Neuron 2021 “NDCil” (ERP-2021-23680733)

BIBLIOGRAPHY

1. Stoodley, C. J. The Cerebellum and Neurodevelopmental Disorders. *The Cerebellum* **15**, 34–37 (2016).
2. Leto, K. *et al.* Consensus Paper: Cerebellar Development. *The Cerebellum* **15**, 789–828 (2016).
3. Garda, A.-L., Echevarría, D. & Martínez, S. Neuroepithelial co-expression of Gbx2 and Otx2 precedes Fgf8 expression in the isthmic organizer. *Mech. Dev.* **101**, 111–118 (2001).
4. Crossley, P. H., Martinez, S. & Martin, G. R. Midbrain development induced by FGF8 in the chick embryo. *Nature* **380**, 66–68 (1996).
5. Chi, C. L., Martinez, S., Wurst, W. & Martin, G. R. The isthmic organizer signal FGF8 is required for cell survival in the prospective midbrain and cerebellum. *Development* **130**, 2633–2644 (2003).
6. Hoshino, M. *et al.* Ptf1a, a bHLH Transcriptional Gene, Defines GABAergic Neuronal Fates in Cerebellum. *Neuron* **47**, 201–213 (2005).
7. Ben-Arie, N. *et al.* Math1 is essential for genesis of cerebellar granule neurons. *Nature* **390**, 169–172 (1997).
8. Machold, R. & Fishell, G. Math1 Is Expressed in Temporally Discrete Pools of Cerebellar Rhombic-Lip Neural Progenitors. *Neuron* **48**, 17–24 (2005).
9. Rakic, P. & Sidman, R. L. Histogenesis of cortical layers in human cerebellum, particularly the lamina dissecans. *J. Comp. Neurol.* **139**, 473–500 (1970).
10. Aldinger, K. A. *et al.* Spatial and cell type transcriptional landscape of human cerebellar development. *Nat. Neurosci.* **24**, 1163–1175 (2021).
11. Minaki, Y., Nakatani, T., Mizuhara, E., Inoue, T. & Ono, Y. Identification of a novel transcriptional corepressor, Corl2, as a cerebellar Purkinje cell-selective marker. *Gene Expr. Patterns* **8**, 418–423 (2008).
12. Sillitoe, R. V. & Joyner, A. L. Morphology, Molecular Codes, and Circuitry Produce the Three-Dimensional Complexity of the Cerebellum. *Annu. Rev. Cell Dev. Biol.* **23**, 549–577 (2007).
13. Haldipur, P. *et al.* Spatiotemporal expansion of primary progenitor zones in the developing human cerebellum. *Science* **366**, 454–460 (2019).
14. Maria, B. L. *et al.* 'Joubert Syndrome' Revisited: Key Ocular Motor Signs With Magnetic Resonance Imaging Correlation. *J. Child Neurol.* **12**, 423–430 (1997).
15. Bachmann-Gagescu, R. *et al.* Healthcare recommendations for Joubert syndrome. *Am. J. Med. Genet. A.* **182**, 229–249 (2020).
16. Bachmann-Gagescu, R. *et al.* Joubert syndrome: a model for untangling recessive disorders with extreme genetic heterogeneity. *J. Med. Genet.* **52**, 514–522 (2015).
17. Serpieri, V. *et al.* Recurrent, founder and hypomorphic variants contribute to the genetic landscape of Joubert syndrome. *J. Med. Genet.* **60**, 885–893 (2023).

18. Mitchison, H. M. & Valente, E. M. Motile and non-motile cilia in human pathology: from function to phenotypes: Motile and non-motile ciliopathies. *J. Pathol.* **241**, 294–309 (2017).
19. Reiter, J. F. & Leroux, M. R. Genes and molecular pathways underpinning ciliopathies. *Nat. Rev. Mol. Cell Biol.* **18**, 533–547 (2017).
20. Mill, P., Christensen, S. T. & Pedersen, L. B. Primary cilia as dynamic and diverse signalling hubs in development and disease. *Nat. Rev. Genet.* **24**, 421–441 (2023).
21. Goetz, S. C. & Anderson, K. V. The primary cilium: a signalling centre during vertebrate development. *Nat. Rev. Genet.* **11**, 331–344 (2010).
22. Reiter, J. F., Blacque, O. E. & Leroux, M. R. The base of the cilium: roles for transition fibres and the transition zone in ciliary formation, maintenance and compartmentalization. *EMBO Rep.* **13**, 608–618 (2012).
23. Jensen, V. L. *et al.* Formation of the transition zone by Mks5/Rpgrip1L establishes a ciliary zone of exclusion (CIZE) that compartmentalises ciliary signalling proteins and controls PIP_2 ciliary abundance. *EMBO J.* **34**, 2537–2556 (2015).
24. Wiegering, A. *et al.* Rpgrip1l controls ciliary gating by ensuring the proper amount of Cep290 at the vertebrate transition zone. *Mol. Biol. Cell* **32**, 675–689 (2021).
25. Besse, L. *et al.* Primary cilia control telencephalic patterning and morphogenesis via Gli3 proteolytic processing. *Development* **138**, 2079–2088 (2011).
26. Andreu-Cervera, A. *et al.* The ciliopathy gene *ftm/rpgrip1l* controls mouse forebrain patterning via region-specific modulation of hedgehog/gli signaling. *J. Neurosci.* 2199–18 (2019) doi:10.1523/JNEUROSCI.2199-18.2019.
27. Chizhikov, V. V. *et al.* Cilia Proteins Control Cerebellar Morphogenesis by Promoting Expansion of the Granule Progenitor Pool. *J. Neurosci.* **27**, 9780–9789 (2007).
28. Spassky, N. *et al.* Primary cilia are required for cerebellar development and Shh-dependent expansion of progenitor pool. *Dev. Biol.* **317**, 246–259 (2008).
29. Aguilar, A. *et al.* Analysis of human samples reveals impaired SHH-dependent cerebellar development in Joubert syndrome/Meckel syndrome. *Proc. Natl. Acad. Sci.* **109**, 16951–16956 (2012).
30. Chang, C.-H. *et al.* Atoh1 Controls Primary Cilia Formation to Allow for SHH-Triggered Granule Neuron Progenitor Proliferation. *Dev. Cell* **48**, 184-199.e5 (2019).
31. Ong, T., Trivedi, N., Wakefield, R., Frase, S. & Solecki, D. J. Siah2 integrates mitogenic and extracellular matrix signals linking neuronal progenitor ciliogenesis with germinal zone occupancy. *Nat. Commun.* **11**, 5312 (2020).
32. Ott, C. M. *et al.* Permanent deconstruction of intracellular primary cilia in differentiating granule cell neurons. *J. Cell Biol.* **223**, e202404038 (2024).
33. Delous, M. *et al.* The ciliary gene RPGRIP1L is mutated in cerebello-oculo-renal syndrome (Joubert syndrome type B) and Meckel syndrome. *Nat. Genet.* **39**, 875–881 (2007).
34. Lancaster, M. A. *et al.* Defective Wnt-dependent cerebellar midline fusion in a mouse model of Joubert syndrome. *Nat. Med.* **17**, 726–731 (2011).
35. Abdelhamed, Z. A. *et al.* The ciliary Frizzled-like receptor Tmem67 regulates canonical

Wnt/β-catenin signalling in the developing cerebellum via Hoxb5. *Sci. Rep.* **9**, 5446 (2019).
36. Damerla, R. R. *et al.* Novel Jbts17 mutant mouse model of Joubert syndrome with cilia transition zone defects and cerebellar and other ciliopathy related anomalies. *Hum. Mol. Genet.* **24**, 3994–4005 (2015).
37. Bashford, A. L. & Subramanian, V. Mice with a conditional deletion of *Talpid3* (*KIAA0586*) – a model for Joubert syndrome. *J. Pathol.* **248**, 396–408 (2019).
38. Suciu, S. K., Long, A. B. & Caspary, T. Smoothened and ARL13B are critical in mouse for superior cerebellar peduncle targeting. *Genetics* **218**, iyab084 (2021).
39. Muguruma, K., Nishiyama, A., Kawakami, H., Hashimoto, K. & Sasai, Y. Self-Organization of Polarized Cerebellar Tissue in 3D Culture of Human Pluripotent Stem Cells. *Cell Rep.* **10**, 537–550 (2015).
40. Silva, T. P. *et al.* Maturation of Human Pluripotent Stem Cell-Derived Cerebellar Neurons in the Absence of Co-culture. *Front. Bioeng. Biotechnol.* **8**, 70 (2020).
41. Silva, T. P. *et al.* Transcriptome profiling of human pluripotent stem cell-derived cerebellar organoids reveals faster commitment under dynamic conditions. *Biotechnol. Bioeng.* **118**, 2781–2803 (2021).
42. Wechsler-Reya, R. J. & Scott, M. P. Control of Neuronal Precursor Proliferation in the Cerebellum by Sonic Hedgehog. *Neuron* **22**, 103–114 (1999).
43. Wiegering, A. *et al.* A differential requirement for ciliary transition zone proteins in human and mouse neural progenitor fate specification. *Nat. Commun.* **16**, 3258 (2025).
44. Richards, S. *et al.* Standards and guidelines for the interpretation of sequence variants: a joint consensus recommendation of the American College of Medical Genetics and Genomics and the Association for Molecular Pathology. *Genet. Med.* **17**, 405–424 (2015).
45. Wiegering, A. *et al.* Cell type-specific regulation of ciliary transition zone assembly in vertebrates. *EMBO J.* **37**, (2018).
46. Taverna, E. & Huttner, W. B. Neural Progenitor Nuclei IN Motion. *Neuron* **67**, 906–914 (2010).
47. Das, R. M. & Storey, K. G. Apical Abscission Alters Cell Polarity and Dismantles the Primary Cilium During Neurogenesis. *Science* **343**, 200–204 (2014).
48. Laguesse, S., Peyre, E. & Nguyen, L. Progenitor genealogy in the developing cerebral cortex. *Cell Tissue Res.* **359**, 17–32 (2015).
49. Sokpor, G., Brand-Saberi, B., Nguyen, H. P. & Tuoc, T. Regulation of Cell Delamination During Cortical Neurodevelopment and Implication for Brain Disorders. *Front. Neurosci.* **16**, 824802 (2022).
50. Gratton, M.-O. *et al.* Hes6 Promotes Cortical Neurogenesis and Inhibits Hes1 Transcription Repression Activity by Multiple Mechanisms. *Mol. Cell. Biol.* **23**, 6922–6935 (2003).
51. Murai, K., Philpott, A. & Jones, P. H. Hes6 Is Required for the Neurogenic Activity of Neurogenin and NeuroD. *PLoS ONE* **6**, e27880 (2011).
52. Behesti, H., Kocabas, A., Buchholz, D. E., Carroll, T. S. & Hatten, M. E. Altered temporal

sequence of transcriptional regulators in the generation of human cerebellar granule cells. *eLife* **10**, e67074 (2021).
53. Long, K. R. & Huttner, W. B. How the extracellular matrix shapes neural development. *Open Biol.* **9**, 180216 (2019).
54. Álvarez, Z. *et al.* Artificial extracellular matrix scaffolds of mobile molecules enhance maturation of human stem cell-derived neurons. *Cell Stem Cell* **30**, 219-238.e14 (2023).
55. Yang, L., Wei, M., Xing, B. & Zhang, C. Extracellular matrix and synapse formation. *Biosci. Rep.* **43**, BSR20212411 (2023).
56. Joyner, A. L., Liu, A. & Millet, S. Otx2, Gbx2 and Fgf8 interact to position and maintain a mid–hindbrain organizer. *Curr. Opin. Cell Biol.* **12**, 736–741 (2000).
57. Sato, T. & Joyner, A. L. The duration of *Fgf8* isthmic organizer expression is key to patterning different tectal-isthmo-cerebellum structures. *Development* **136**, 3617–3626 (2009).
58. Green, M. J. *et al.* Independently specified *Atoh1* domains define novel developmental compartments in rhombomere 1. *Development* **141**, 389–398 (2014).
59. Suzuki-Hirano, A., Harada, H., Sato, T. & Nakamura, H. Activation of Ras-ERK pathway by Fgf8 and its downregulation by Sprouty2 for the isthmus organizing activity. *Dev. Biol.* **337**, 284–293 (2010).
60. Yu, T., Yaguchi, Y., Echevarria, D., Martinez, S. & Basson, M. A. Sprouty genes prevent excessive FGF signalling in multiple cell types throughout development of the cerebellum. *Development* **138**, 2957–2968 (2011).
61. Del Corral, R. D., Breitkreuz, D. N. & Storey, K. G. Onset of neuronal differentiation is regulated by paraxial mesoderm and requires attenuation of FGF signalling. *Development* **129**, 1681–1691 (2002).
62. Wilcock, A. C., Swedlow, J. R. & Storey, K. G. Mitotic spindle orientation distinguishes stem cell and terminal modes of neuron production in the early spinal cord. *Development* **134**, 1943–1954 (2007).
63. Olivera-Martinez, I. & Storey, K. G. Wnt signals provide a timing mechanism for the FGF-retinoid differentiation switch during vertebrate body axis extension. *Development* **134**, 2125–2135 (2007).
64. Lukaszewicz, A., Savatier, P., Cortay, V., Kennedy, H. & Dehay, C. Contrasting Effects of Basic Fibroblast Growth Factor and Neurotrophin 3 on Cell Cycle Kinetics of Mouse Cortical Stem Cells. *J. Neurosci.* **22**, 6610–6622 (2002).
65. Gantner, C. W. *et al.* FGF-MAPK signaling regulates human deep-layer corticogenesis. *Stem Cell Rep.* **16**, 1262–1275 (2021).
66. Basson, M. A. *et al.* Specific regions within the embryonic midbrain and cerebellum require different levels of FGF signaling during development. *Development* **136**, 1962–1962 (2009).
67. Catala, M. Development of the Central Nervous System. in *Textbook of Pediatric Neurosurgery* (eds. Di Rocco, C., Pang, D. & Rutka, J. T.) 1–99 (Springer International Publishing, Cham, 2019). doi:10.1007/978-3-319-31512-6_1-1.

68. Watson, C., Shimogori, T. & Puelles, L. Mouse *Fgf8* -Cre-LacZ lineage analysis defines the territory of the postnatal mammalian isthmus. *J. Comp. Neurol.* **525**, 2782–2799 (2017).
69. Hämmerle, B. *et al.* Transient expression of Mnb/Dyrk1a couples cell cycle exit and differentiation of neuronal precursors by inducing p27KIP1 expression and suppressing NOTCH signaling. *Development* **138**, 2543–2554 (2011).
70. Roepman, R. *et al.* Interaction of nephrocystin-4 and RPGRIP1 is disrupted by nephronophthisis or Leber congenital amaurosis-associated mutations. *Proc. Natl. Acad. Sci.* **102**, 18520–18525 (2005).
71. Arts, H. H. *et al.* Mutations in the gene encoding the basal body protein RPGRIP1L, a nephrocystin-4 interactor, cause Joubert syndrome. *Nat. Genet.* **39**, 882–888 (2007).
72. Sang, L. *et al.* Mapping the NPHP-JBTS-MKS Protein Network Reveals Ciliopathy Disease Genes and Pathways. *Cell* **145**, 513–528 (2011).
73. Arellano, J. I., Guadiana, S. M., Breunig, J. J., Rakic, P. & Sarkisian, M. R. Development and distribution of neuronal cilia in mouse neocortex. *J. Comp. Neurol.* **520**, 848–873 (2012).
74. Wu, J. Y. *et al.* Mapping of neuronal and glial primary cilia contactome and connectome in the human cerebral cortex. *Neuron* **112**, 41-55.e3 (2024).
75. Aoto, K., Nishimura, T., Eto, K. & Motoyama, J. Mouse GLI3 Regulates Fgf8 Expression and Apoptosis in the Developing Neural Tube, Face, and Limb Bud. *Dev. Biol.* **251**, 320–332 (2002).
76. Jiwani, T., Kim, J. J. & Rosenblum, N. D. Suppressor of Fused (Sufu) controls cerebellum granule cell proliferation by suppressing Fgf8 and spatially regulating Gli proteins. *Development* dev.170274 (2020) doi:10.1242/dev.170274.
77. Fleck, J. S. *et al.* Inferring and perturbing cell fate regulomes in human brain organoids. *Nature* **621**, 365–372 (2023).
78. Dobin, A. *et al.* STAR: ultrafast universal RNA-seq aligner. *Bioinformatics* **29**, 15–21 (2013).
79. Ewels, P., Magnusson, M., Lundin, S. & Käller, M. MultiQC: summarize analysis results for multiple tools and samples in a single report. *Bioinformatics* **32**, 3047–3048 (2016).
80. Liao, Y., Smyth, G. K. & Shi, W. featureCounts: an efficient general purpose program for assigning sequence reads to genomic features. *Bioinformatics* **30**, 923–930 (2014).
81. Lê, S., Josse, J. & Husson, F. FactoMineR: An R Package for Multivariate Analysis. *J. Stat. Softw.* **25**, 1–18 (2008).
82. Love, M. I., Huber, W. & Anders, S. Moderated estimation of fold change and dispersion for RNA-seq data with DESeq2. *Genome Biol.* **15**, 550 (2014).
83. Zink, R. C., Wolfinger, R. D. & Mann, G. Summarizing the incidence of adverse events using volcano plots and time intervals. *Clin. Trials* **10**, 398–406 (2013).
84. Zhou, Y. *et al.* Metascape provides a biologist-oriented resource for the analysis of systems-level datasets. *Nat. Commun.* **10**, 1523 (2019).

Figure 1

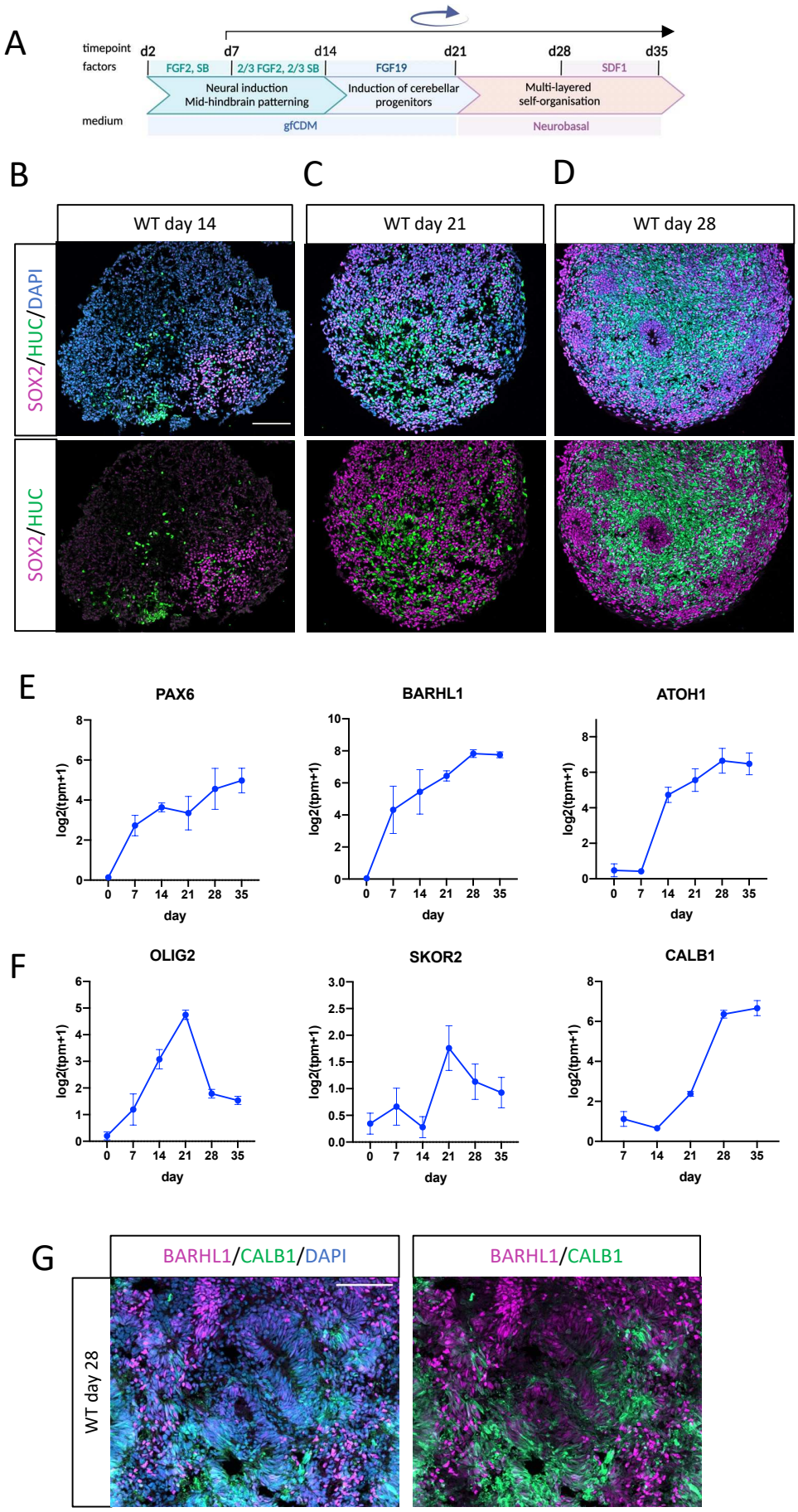
A
timepoint
factors
medium
d2
d7
d14
d21
d28
d35
FGF2, SB
2/3 FGF2, 2/3 SB
FGF19
SDF1
Neural induction
Mid-hindbrain patterning
Induction of cerebellar
progenitors
Multi-layered
self-organisation
gfCDM
Neurobasal
B
C
D
WT day 14
WT day 21
WT day 28
SOX2/HUC/DAPI
SOX2/HUC
E
PAX6
BARHL1
ATOH1
log2(tpm+1)
day
F
OLIG2
SKOR2
CALB1
G
BARHL1/CALB1/DAPI
BARHL1/CALB1
WT day 28

FIGURE 1. Cerebellar organoids generated from human induced pluripotent stem cells recapitulate early steps of cerebellar development

(A) Diagram of the 3D cerebellar differentiation protocol. Time-line and drugs (SB: SMAD antagonists SB-431542; FGF2: Fibroblast growth factor 2; FGF19: Fibroblast growth factor 19; SDF1: stromal cell-derived factor 1) are indicated on top, culture media at the bottom. The blue circular arrow on top indicates orbital rotation. Modified after [1]. **(B-D)** Immunofluorescence for SOX2 (magenta, neural progenitors) and HUC/D (green, early-born neurons) on cryosections from WT organoids at indicated time points. **(E, F)** Graphs showing the RNA expression levels of cerebellar markers in WT organoids along the differentiation protocol, based on the mean ± SEM of the Log2(tpm+1) values from the bulk RNASeq (N=4 independent experiments: N=3 Ph2 line, N=1 Wtc11 line; n>20 organoids per condition), (E) Granule Cell Progenitor (GCP) markers (*ATOH1, BARHL1* and *PAX6*) and (F) Purkinje Cell (PC) markers (*OLIG2, SKOR2* and *CALB1*). **(G)** Immunofluorescence for BARHL1 (GCP marker) and CALB1 (PC marker) on day 28 WT organoid cryosection. Scale bars: 100 µm in B-D and G.

Figure 2

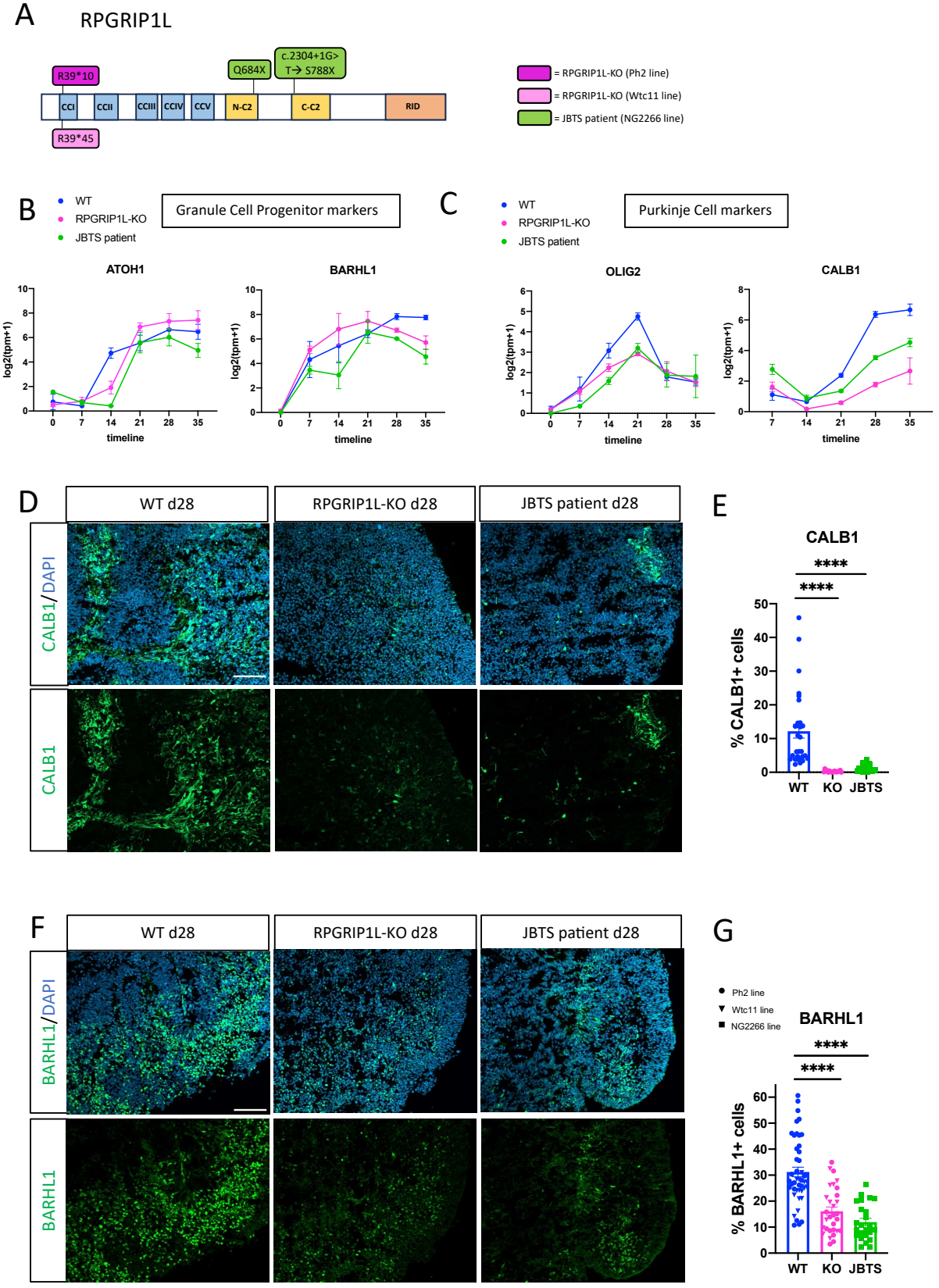
A
RPGRIP1L
R39*10
R39*45
Q684X
c.2304+1G>T→ S788X
CCI
CCII
CCIII
CCIV
CCV
N-C2
C-C2
RID
= RPGRIP1L-KO (Ph2 line)
= RPGRIP1L-KO (Wtc11 line)
= JBTS patient (NG2266 line)
B
WT
RPGRIP1L-KO
JBTS patient
Granule Cell Progenitor markers
ATOH1
BARHL1
log2(tpm+1)
timeline
C
Purkinje Cell markers
OLIG2
CALB1
D
WT d28
RPGRIP1L-KO d28
JBTS patient d28
CALB1/DAPI
CALB1
E
CALB1
****
% CALB1+ cells
WT
KO
JBTS
F
BARHL1/DAPI
BARHL1
G
Ph2 line
Wtc11 line
NG2266 line
BARHL1
% BARHL1+ cells

FIGURE 2. *RPGRIP1L* KO and JBTS patient-derived cerebellar organoids present severe reduction of Purkinje Cell markers and a mild decrease of Granule Cell Progenitor markers

(A) Schematic representation of the RPGRIP1L protein and relative position of the mutations present in each hiPSC line used. In both *RPGRIP1L* KO lines (Ph2 clone #44, in purple; Wtc11 clone #65, in pink) homozygous frameshift mutations result in premature stop codon before the first coiled-coil domain of RPGRIP1L. JBTS patient (NG2266 in green) variants p.Q684X and c.2304+1G>T result in stop codons between the first and the second RPGRIP1L C2 domain. **(B, C)** Graphs showing temporal gene expression analysis of GCP (*ATOH1* and *BARHL1*) (B) and PC (*OLIG2* and *CALB1*) lineage markers (C) in WT (blue curve), *RPGRIP1L* KO (magenta curve), and JBTS patient (green curve) cerebellar organoids along the differentiation protocol. n>20 organoids per condition per experiment are collected (WT and *RPGRIP1L* KO: Ph2 N=3, Wtc11 N=1; JBTS patient: NG2266 N=2). Log2(tpm+1) values from bulk RNASeq analysis are displayed as mean ± SEM. **(D)** Immunofluorescence for CALB1 (PC marker) on cryosections from day 28 WT, *RPGRIP1L* KO and JBTS patient organoids. **(E)** Quantification showing the % of CALB1-positive cells over the total number of nuclei stained with DAPI. Positive cells were counted in more than 15 sections from different organoids per experiment per condition (WT and *RPGRIP1L* KO: Ph2 line N=2 – round dots; JBTS patient: NG2266 line N=2 – squared dots). Data are shown as mean ± SEM. Asterisks denote statistical significance according to One-Way ANOVA Kruskal-Wallis test with Dunn's correction (****P<0.0001). **(F)** Immunofluorescence for BARHL1 (GCP marker) on cryosections from day 28 WT, *RPGRIP1L* KO and JBTS patient organoids. **(G)** Quantification showing the % of BARHL1-positive cells over the total number of nuclei stained with DAPI. Positive cells were counted in more than 15 sections from different organoids per experiment per condition (WT and *RPGRIP1L* KO: Ph2 line N=2 – round dots , Wtc11 line N=1 – triangular dots; JBTS patient: NG2266 line N=2 – squared dots). Data are shown as mean ± SEM. Asterisks denote statistical significance according to One-Way ANOVA Kruskal-Wallis test with Dunn's correction (****P<0.0001). N: number of independent experimental replicates. Scale bars: 100 µm in D and F.

.

Figure 3

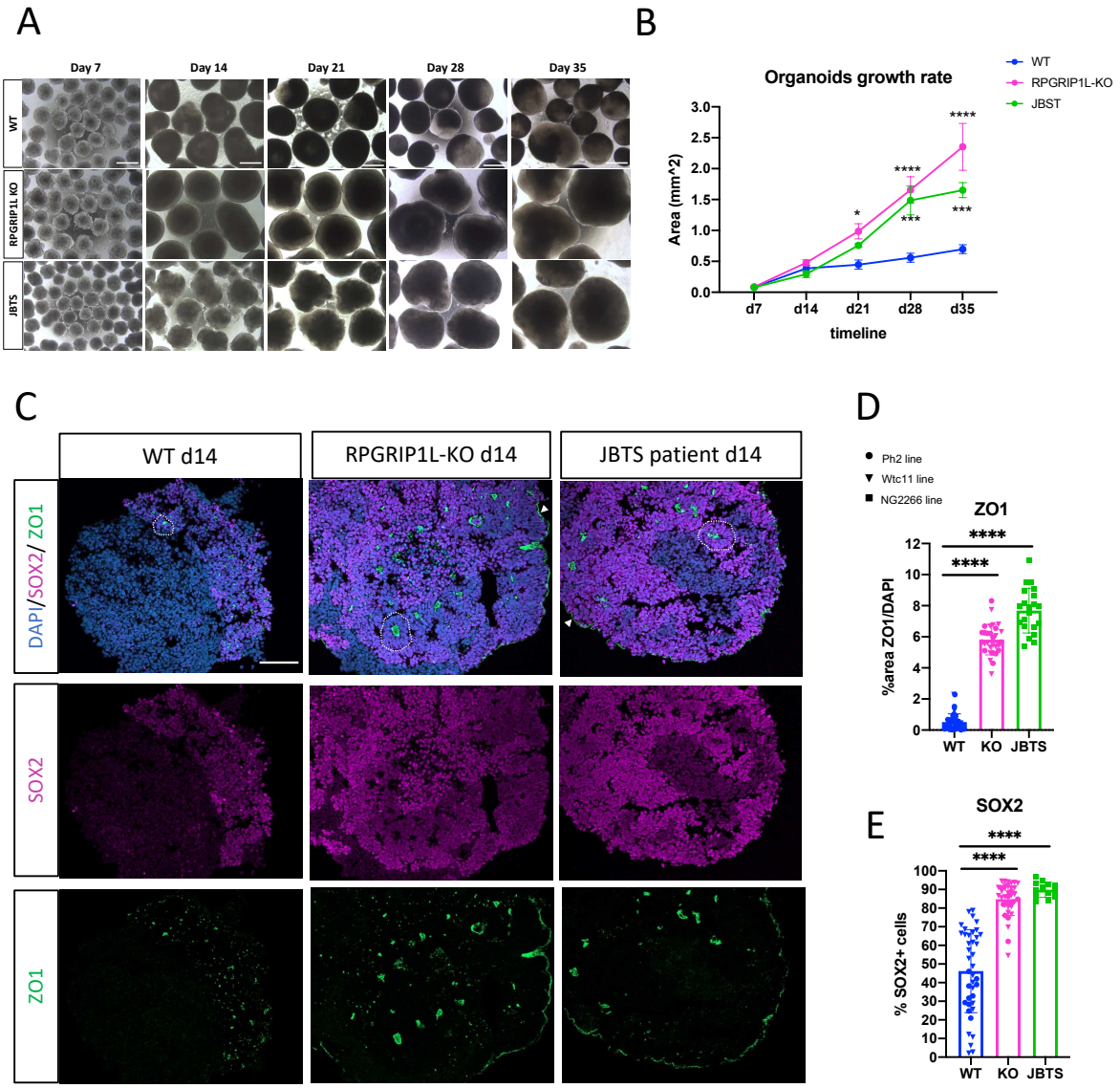
A
Day 7
Day 14
Day 21
Day 28
Day 35
WT
RPGRIP1L KO
JBTS
B
Organoids growth rate
WT
RPGRIP1L-KO
JBST
Area (mm^2)
timeline
d7
d14
d21
d28
d35
C
WT d14
RPGRIP1L-KO d14
JBTS patient d14
DAPI/SOX2/ ZO1
SOX2
ZO1
D
Ph2 line
Wtc11 line
NG2266 line
ZO1
%area ZO1/DAPI
WT
KO
JBTS
E
SOX2
% SOX2+ cells
WT
KO
JBTS

FIGURE 3. Organoid size and area covered by SOX2$^+$/ZO1$^+$ progenitors are both increased in *RPGRIP1L* cerebellar organoids.

(A) Representative bright field images of cerebellar organoids at the indicated time points. **(B)** Graph representing the growth rate of cerebellar organoids. Organoid area was measured every 7 days from day 7 to day 35 of the differentiation protocol. Data are shown as the mean ± SEM of average organoid area from several independent experiment (N=3 Ph2 line, N=3 Wtc11 line, N=3 NG2266 line, n=10-60 organoids analyzed per experiment per condition). For WT and *RPGRIP1L* KO conditions, data from Ph2 and Wtc11 lines were pooled. Asterisks denote statistical significance according to Two-Way ANOVA test (*P<0.033, ***P<0.0002, ****P<0.0001). **(C)** Immunofluorescence for SOX2 neural progenitor marker (in magenta) and for ZO1 apical marker (in green) on cryosections from WT, *RPGRIP1L* KO and JBTS patient organoids at day 14. Examples of neural rosettes are circled by dotted lines **(D)** Quantification of the ZO1 positive area over the DAPI positive area in sections from WT, *RPGRIP1L* KO and JBTS patient organoids at day 14. Data are shown as mean ± SEM, from 20-30 organoids from independent experiments and hiPSC lines (WT and *RPGRIP1L* KO: Ph2 N=1 – round dots, Wtc11 N=1 – triangular dots; JBTS patient: NG2266 N=1 – squared dots). Asterisks denote statistical significance according to One-Way ANOVA Kruskal-Wallis test with Dunn's correction (****P< 0.0001) **(E)** Graph showing the % of SOX2$^+$ cells in sections from WT, *RPGRIP1L* KO and JBTS patient organoids at day 14. Data are presented as mean ± SEM, from 10-40 organoids from independent experiments and hiPSC lines (WT and *RPGRIP1L* KO: Ph2 N=1 – round dots, Wtc11 N=2 – triangular dots; JBTS patient: NG2266 N=1 – squared dots). Asterisks denote statistical significance according to One-Way ANOVA Kruskal-Wallis test with Dunn's correction (****P< 0.0001). N: number of independent experimental replicates. Scale bars: 500 µm in A and 100 µm in C.

Figure 4

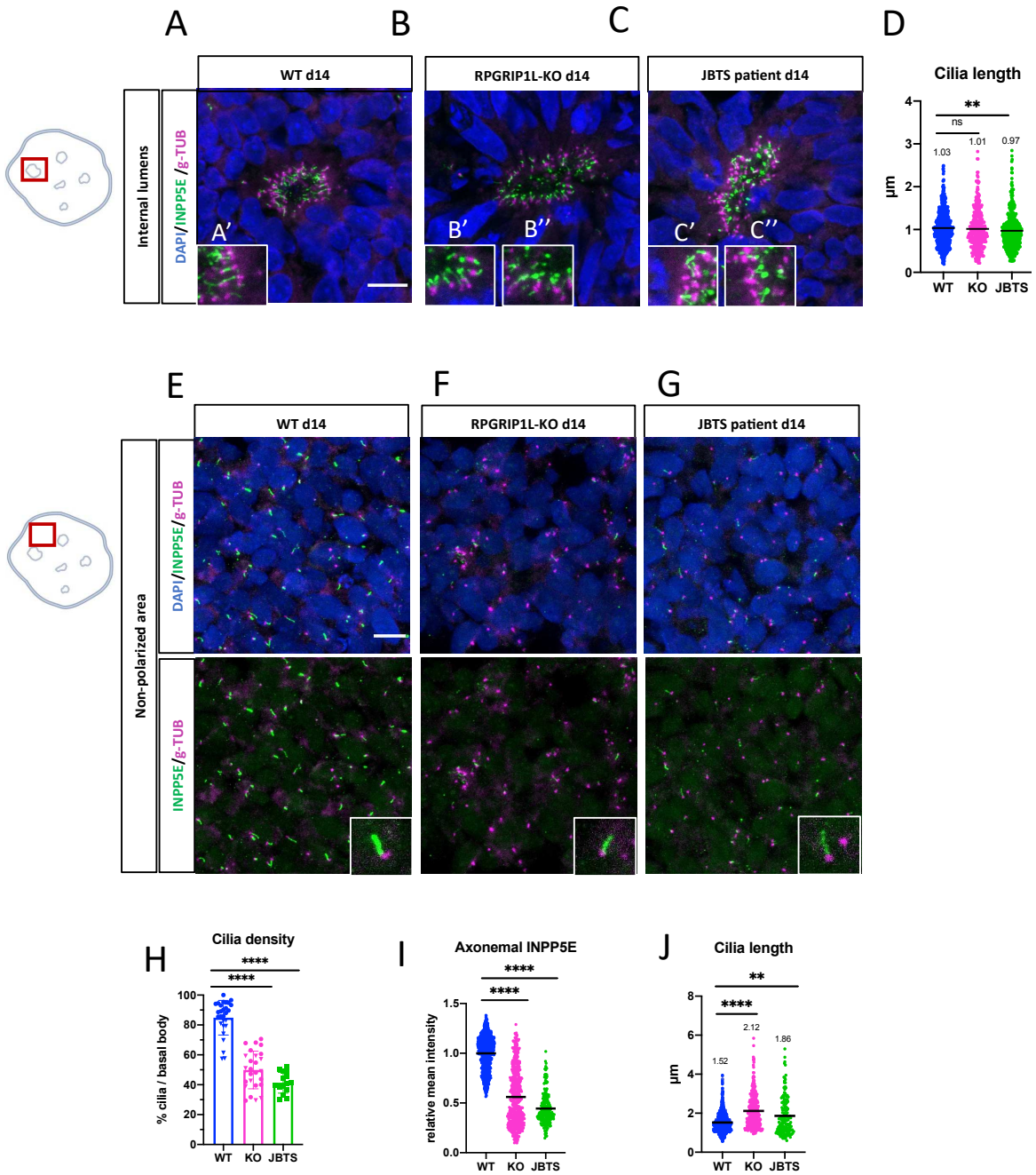
A
B
C
D
WT d14
RPGRIP1L-KO d14
JBTS patient d14
Internal lumens
DAPI/INPP5E /g-TUB
A'
B'
B''
C'
C''
Cilia length
**
ns
1.03
1.01
0.97
µm
WT
KO
JBTS
E
F
G
Non-polarized area
INPP5E/g-TUB
H
Cilia density
****
% cilia / basal body
I
Axonemal INPP5E
relative mean intensity
J
Cilia length
1.52
2.12
1.86

FIGURE 4. Differential requirement of RPGRIP1L protein for ciliogenesis in apical and non-polarized neural progenitors.

(A-C) Immunofluorescence for the ciliary protein INPP5E (in green) and the basal body marker gamma-TUBULIN (in magenta) on sections from WT (A), *RPGRIP1L* KO (B) and JBTS patient (C) cerebellar organoids at day 14. Scale bar, 10 µm. The schematic on the left represents the position of the scanned regions: i.e. internal lumen of neural rosettes. **(D)** Graph showing the quantification of ciliary length. Measures for individual cilia are represented and the mean value is indicated. Asterisks denote statistical significance according to One-Way ANOVA Kruskal-Wallis and Dunn's test (**P < 0.0021)**. (E-G)** Immunofluorescence for ciliary axonemes (labeled by INPP5E in green) and basal bodies (labeled by gamma-TUBULIN in magenta) on sections from WT (E), *RPGRIP1L* KO (F) and JBTS patient (G) cerebellar organoids at day 14. Scale bar, 10 µm. The schematic on the left represents the position of the scanned regions: i.e. non-polarized tissue. **(H-I-J)** Graphs showing quantifications of ciliary properties in non-polarized areas of WT, *RPGRIP1L* KO and JBTS patient cerebellar organoids. Asterisks denote statistical significance according to One-Way ANOVA Kruskal-Wallis and Dunn's test (**P < 0.0021, ****P < 0.0001). In **(H)** data are shown as the mean ± SEM. Ciliary density is calculated as the number of INPP5E+ axonemes over the total number of gamma-TUBULIN basal bodies per field. Each dot on the graph represents one quantified field representative for one organoid section. Data from >15 organoids from independent experiments and hiPSC lines (WT and *RPGRIP1L* KO: Ph2 N=1, Wtc11 N=1; JBTS patient: NG2266 N=1). In **(I-J)** each dot on the graph represents one individual cilium. Average axonemal INPP5E intensity after background subtraction (I) and average cilia length (J) are calculated from >200 cilia measured in >15 organoids from independent experiments and hiPSC lines (WT and *RPGRIP1L* KO: Ph2 N=1, Wtc11 N=1; JBTS patient: NG2266 N=1). N: number of independent experimental replicates. Scale bars: 10 µm in A-C and E-G.

Figure 5

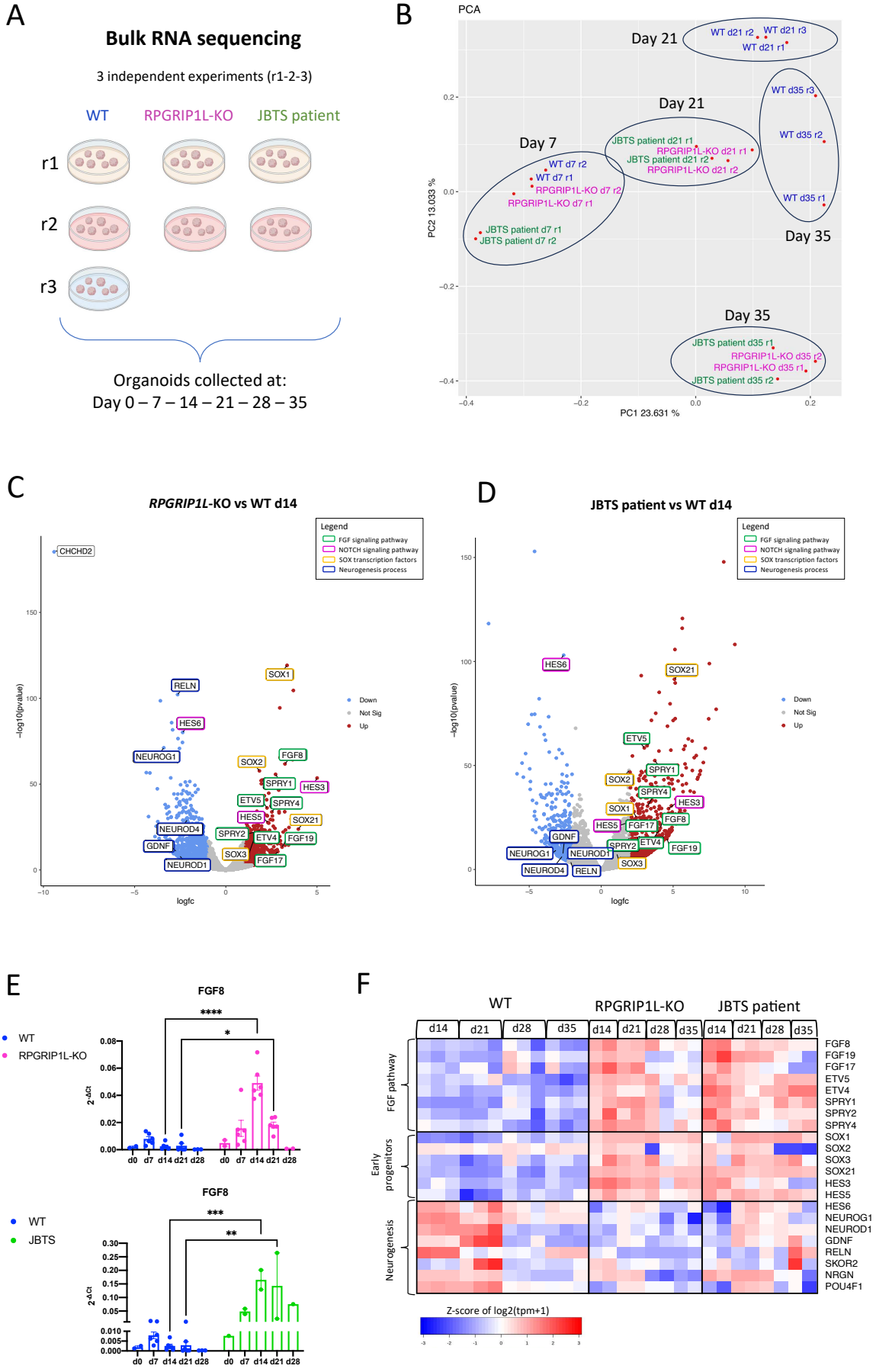
A
Bulk RNA sequencing
3 independent experiments (r1-2-3)
WT
RPGRIP1L-KO
JBTS patient
r1
r2
r3
Organoids collected at:
Day 0 – 7 – 14 – 21 – 28 – 35
B
PCA
Day 21
WT d21 r2
WT d21 r3
WT d21 r1
Day 21
WT d35 r3
WT d35 r2
WT d35 r1
Day 35
Day 7
JBTS patient d21 r1
RPGRIP1L-KO d21 r1
JBTS patient d21 r2
RPGRIP1L-KO d21 r2
WT d7 r2
WT d7 r1
RPGRIP1L-KO d7 r2
RPGRIP1L-KO d7 r1
JBTS patient d7 r1
JBTS patient d7 r2
Day 35
JBTS patient d35 r1
RPGRIP1L-KO d35 r2
RPGRIP1L-KO d35 r1
JBTS patient d35 r2
PC2 13.033 %
PC1 23.631 %
C
RPGRIP1L-KO vs WT d14
Legend
FGF signaling pathway
NOTCH signaling pathway
SOX transcription factors
Neurogenesis process
Down
Not Sig
Up
CHCHD2
RELN
HES6
NEUROG1
NEUROD4
GDNF
NEUROD1
SOX1
SOX2
FGF8
SPRY1
HES3
ETV5
SPRY4
HES5
SOX21
SPRY2
ETV4
FGF19
SOX3
FGF17
−log10(pvalue)
logfc
D
JBTS patient vs WT d14
Legend
FGF signaling pathway
NOTCH signaling pathway
SOX transcription factors
Neurogenesis process
Down
Not Sig
Up
HES6
SOX21
ETV5
SPRY1
SOX2
SPRY4
HES3
SOX1
FGF8
HES5
FGF17
GDNF
ETV4
SPRY2
FGF19
NEUROG1
NEUROD1
SOX3
NEUROD4
RELN
−log10(pvalue)
logfc
E
FGF8
WT
RPGRIP1L-KO
****
*
2^-ΔCt
d0 d7 d14 d21 d28 d0 d7 d14 d21 d28
FGF8
WT
JBTS
***
**
2^-ΔCt
d0 d7 d14 d21 d28 d0 d7 d14 d21 d28
F
WT
RPGRIP1L-KO
JBTS patient
d14 d21 d28 d35 d14 d21 d28 d35 d14 d21 d28 d35
FGF pathway
Early progenitors
Neurogenesis
FGF8
FGF19
FGF17
ETV5
ETV4
SPRY1
SPRY2
SPRY4
SOX1
SOX2
SOX3
SOX21
HES3
HES5
HES6
NEUROG1
NEUROD1
GDNF
RELN
SKOR2
NRGN
POU4F1
Z-score of log2(tpm+1)

FIGURE 5. Transcriptome analysis revealed early FGF signaling upregulation and neurogenesis impairment in *RPGRIP1L*-deficient cerebellar organoids

(A) Schematic representation of the samples used in bulk RNA sequencing. Genotypes, timepoints and experimental replicates are indicated for the Ph2 hiPSC line (WT and *RPGRIP1L* KO) and NG2266 hiPSC line (JBTS patient). **(B)** PCA analysis performed on WT, *RPGRIP1L* KO and JBTS patient samples showing the transcriptome variation across time and genotypes. **(C-D)** Volcano plots representing differentially expressed genes (DEGs) resulting from DESeq2 analysis (only genes with $P<0.001$; $|\log_2 FC|>2$ are colored) in *RPGRIP1L* KO versus WT condition (C) or in JBTS patient versus WT condition (D) at day 14. Selected genes from representative pathways and cellular processes are circled with different colors as indicated in the legend on the top right of the panel. **(E)** qPCR analysis of *FGF8* expression levels on cerebellar organoids at different timepoints (WT and *RPGRIP1L* KO: Ph2 N=2, Wtc11 N=4; JBTS patient: NG2266 N=2). Data are shown as mean ± SEM. Asterisks denote statistical significance according to ordinary Two-Way ANOVA performed on WT and *RPGRIP1L* KO samples (*$P<0.033$, ****$P < 0.0001$). **(F)** Heatmap showing the z-score of the log 2(tpm+1) values of selected differentially expressed genes in WT and *RPGRIP1L*-deficient cerebellar organoids over time (WT: N=3; *RPGRIP1L* KO: N=2, JBTS patient: N=2). N: number of independent experimental replicates.

Figure 6

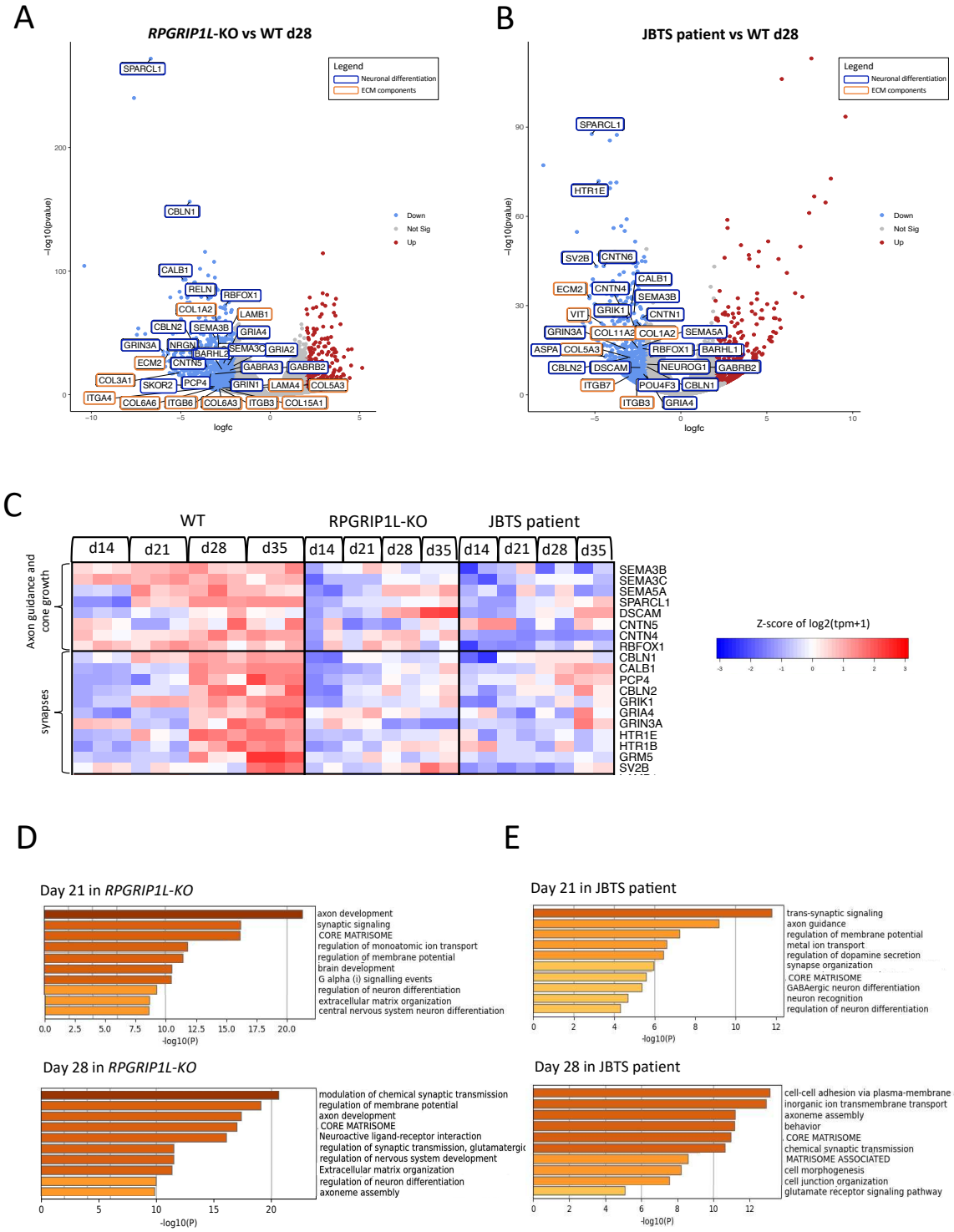
A
RPGRIP1L-KO vs WT d28
Legend
Neuronal differentiation
ECM components
Down
Not Sig
Up
−log10(pvalue)
logfc
SPARCL1
CBLN1
CALB1
RELN
RBFOX1
COL1A2
LAMB1
CBLN2
SEMA3B
GRIA4
GRIN3A
NRGN
BARHL2
SEMA3C
GRIA2
ECM2
CNTN5
GABRA3
GABRB2
COL3A1
SKOR2
PCP4
GRIN1
LAMA4
COL5A3
ITGA4
COL6A6
ITGB6
COL6A3
ITGB3
COL15A1
B
JBTS patient vs WT d28
SPARCL1
HTR1E
SV2B
CNTN6
CALB1
ECM2
CNTN4
SEMA3B
VIT
GRIK1
CNTN1
GRIN3A
COL11A2
COL1A2
SEMA5A
ASPA
COL5A3
RBFOX1
BARHL1
CBLN2
DSCAM
NEUROG1
GABRB2
ITGB7
POU4F3
CBLN1
ITGB3
GRIA4
C
WT
RPGRIP1L-KO
JBTS patient
d14
d21
d28
d35
Axon guidance and cone growth
synapses
SEMA3B
SEMA3C
SEMA5A
SPARCL1
DSCAM
CNTN5
CNTN4
RBFOX1
CBLN1
CALB1
PCP4
CBLN2
GRIK1
GRIA4
GRIN3A
HTR1E
HTR1B
GRM5
SV2B
Z-score of log2(tpm+1)
D
Day 21 in RPGRIP1L-KO
axon development
synaptic signaling
CORE MATRISOME
regulation of monoatomic ion transport
regulation of membrane potential
brain development
G alpha (i) signalling events
regulation of neuron differentiation
extracellular matrix organization
central nervous system neuron differentiation
-log10(P)
Day 28 in RPGRIP1L-KO
modulation of chemical synaptic transmission
regulation of membrane potential
axon development
CORE MATRISOME
Neuroactive ligand-receptor interaction
regulation of synaptic transmission, glutamatergic
regulation of nervous system development
Extracellular matrix organization
regulation of neuron differentiation
axoneme assembly
-log10(P)
E
Day 21 in JBTS patient
trans-synaptic signaling
axon guidance
regulation of membrane potential
metal ion transport
regulation of dopamine secretion
synapse organization
CORE MATRISOME
GABAergic neuron differentiation
neuron recognition
regulation of neuron differentiation
-log10(P)
Day 28 in JBTS patient
cell-cell adhesion via plasma-membrane
inorganic ion transmembrane transport
axoneme assembly
behavior
CORE MATRISOME
chemical synaptic transmission
MATRISOME ASSOCIATED
cell morphogenesis
cell junction organization
glutamate receptor signaling pathway
-log10(P)

FIGURE 6. *RPGRIP1L*-deficient organoids display severe neuronal maturation and extracellular matrix defects as shown by transcriptome analysis

(A-B) Volcano plots representing differentially expressed genes (DEGs) resulting from DESeq2 analysis (only genes with $P<0.001, |\log_2 FC|>2$ are colored) in *RPGRIP1L* KO versus WT condition (A) or in JBTS patient versus WT condition (B) at day 28. Selected genes involved in neuronal differentiation or in building ECM are circled with different colors as indicated in the legend on the top right of the panel. **(C)** Heatmap showing the z-score of the log 2(tpm+1) values of selected differentially expressed genes in WT and *RPGRIP1L*-deficient cerebellar organoids over time (WT: N=3; *RPGRIP1L* KO: N=2, JBTS patient: N=2). **(D-E)** Selected GO-terms overrepresented among *RPGRIP1L* KO (D) and JBTS patient (E) downregulated genes extracted from bulk RNA seq DESeq2 lists at day 21 and 28. N: number of independent experimental replicates.

Figure 7

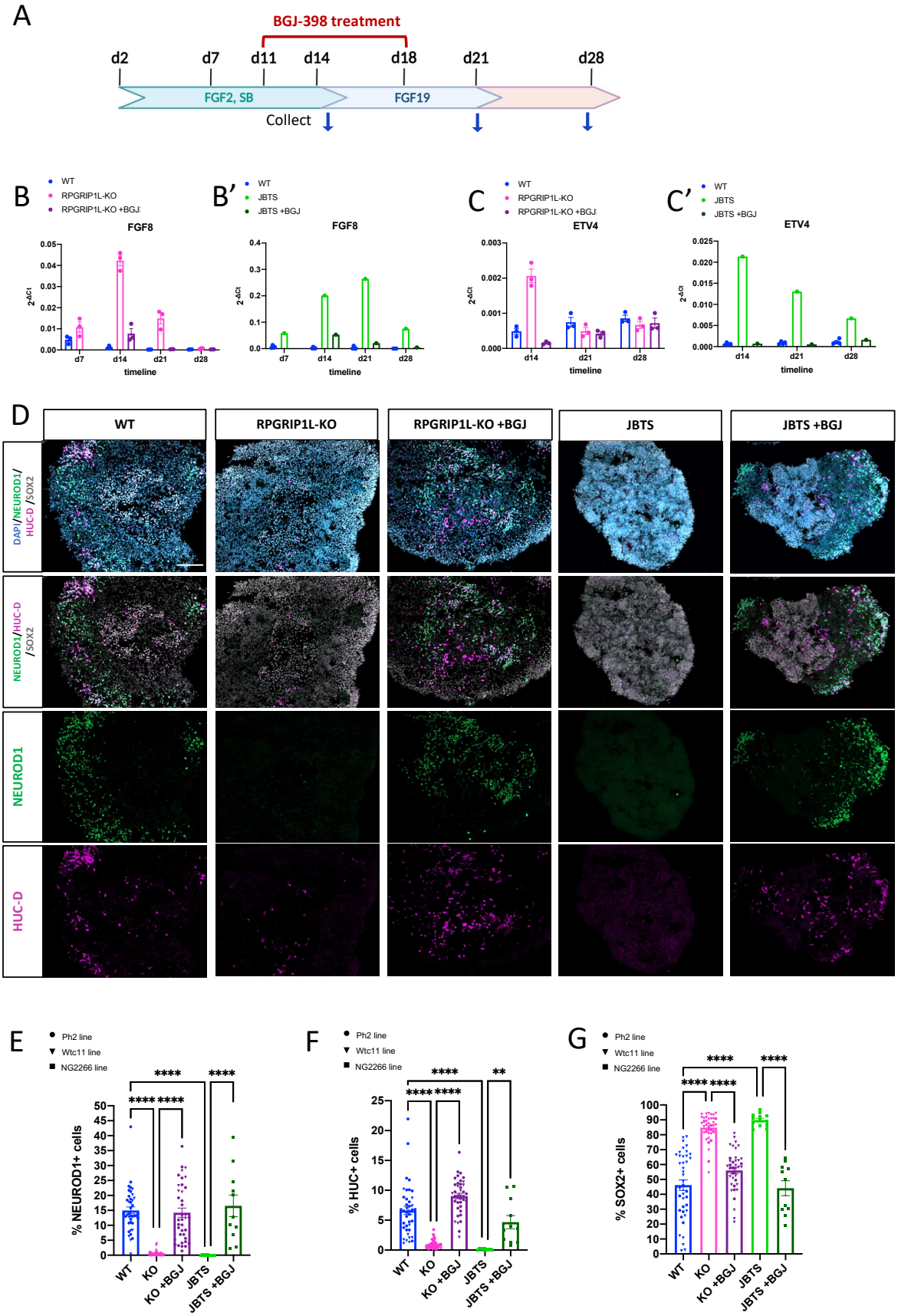
A
BGJ-398 treatment
d2
d7
d11
d14
d18
d21
d28
FGF2, SB
FGF19
Collect
B
WT
RPGRIP1L-KO
RPGRIP1L-KO +BGJ
FGF8
timeline
B'
JBTS
JBTS +BGJ
C
ETV4
C'
D
WT
RPGRIP1L-KO
RPGRIP1L-KO +BGJ
JBTS
JBTS +BGJ
DAPI/NEUROD1/HUC-D /SOX2
NEUROD1/HUC-D /SOX2
NEUROD1
HUC-D
E
Ph2 line
Wtc11 line
NG2266 line
% NEUROD1+ cells
F
% HUC+ cells
G
% SOX2+ cells

FIGURE 7. Blocking FGF signaling with BGJ-398 rescues neurogenesis in *RPGRIP1L* KO cerebellar organoids

(A) Scheme representing the experimental plan for organoid treatment with FGFR-inhibitor (BGJ-398) along the 3D cerebellar differentiation protocol. Arrows on the top represent the timepoints of BGJ-398 pulses. Arrows at the bottom indicate the timepoints at which organoids were collected after receiving BGJ-398 treatment. **(B-C)** Graphs showing the expression levels (qPCR analysis) of FGF8 and ETV4 in WT (blue dots), *RPGRIP1L* KO (pink dots) and *RPGRIP1L* KO+BGJ-398 (violet dots) organoids at different timepoints (Wtc11 N=3). Data are shown as mean ± SEM. **(B'-C')** Graphs showing the expression levels (qPCR analysis) of FGF8 and ETV4 in WT (blue dots), JBTS (bright green dots) and JBTS+BGJ-398 (dark green dots) organoids at different timepoints (WT N=3, JBTS N=1). Data are shown as mean ± SEM. **(D)** Immunofluorescence for SOX2 (in gray), NEUROD1 (in green) and HUC/D (in magenta) on cryosections from WT, *RPGRIP1L*-deficient and *RPGRIP1L*-deficient +BGJ-398 organoids at day 14. Scale bar, 100 µm. **(E-F-G)** Graphs showing the % of NEUROD1-positive cells (E), HUC/D positive cells (F) and SOX2-positive cells (G) over the total number of nuclei stained with DAPI. Positive cells were counted in more than 15 sections from different organoids per condition (WT and *RPGRIP1L* KO: Ph2 N=1 – circular dots, Wtc11 N=2 – triangular dots; JBTS: NG2266 N=1 squared dots). Each dot in the graph represents one organoid; mean ± SEM are shown. Asterisks denote statistical significance according to One-Way ANOVA Kruskal-Wallis test with Dunn's correction (**P<0.0021; ****P<0.0001). N: number of independent experimental replicates.

Figure 8

A

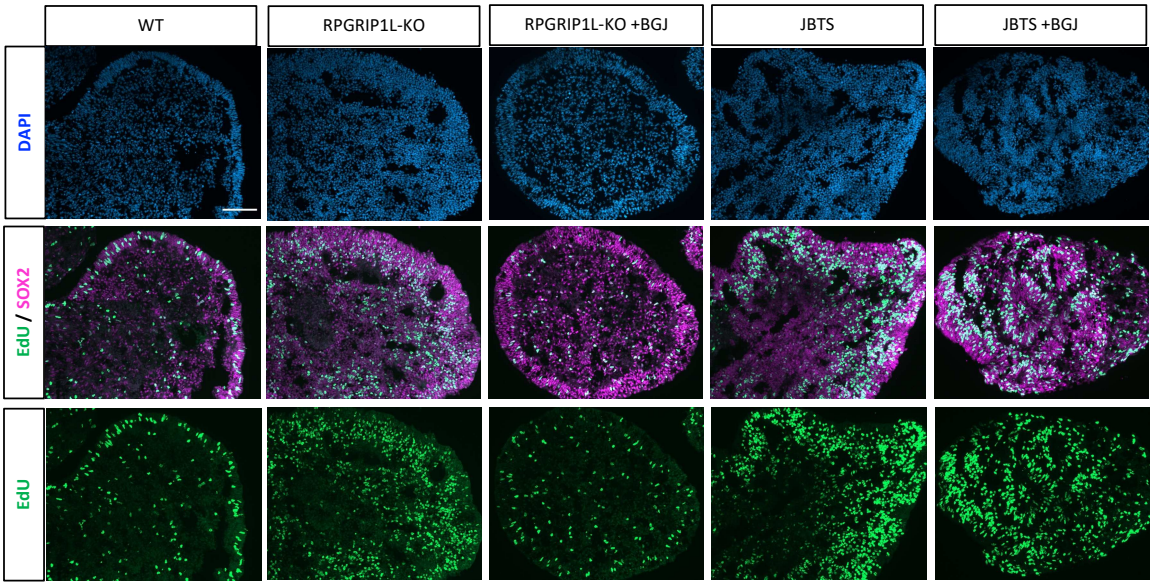

B

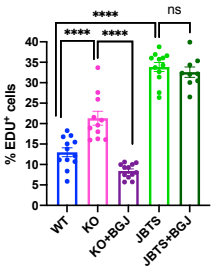

C

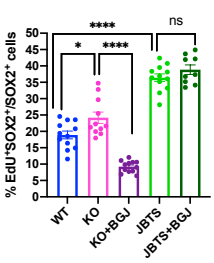

D

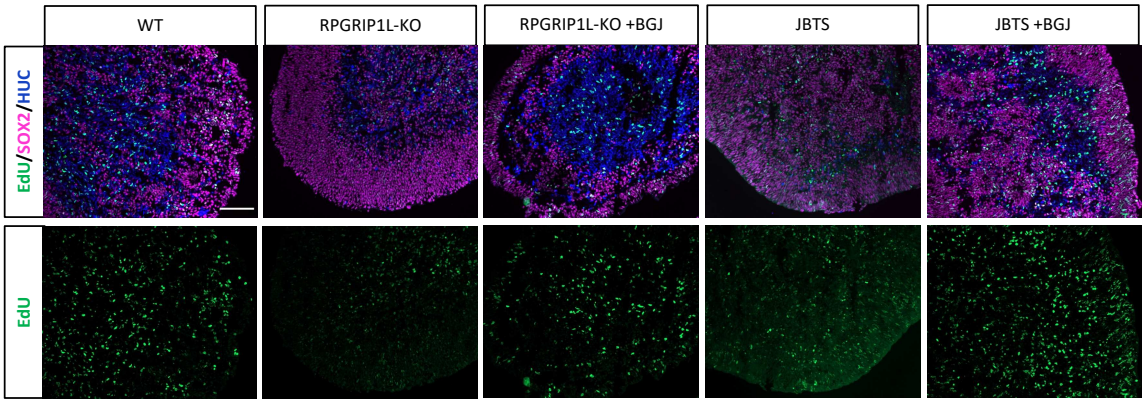

E

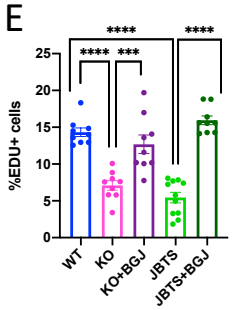

F

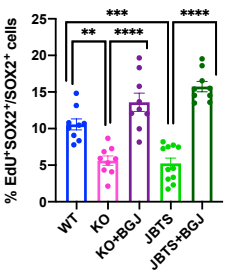

G

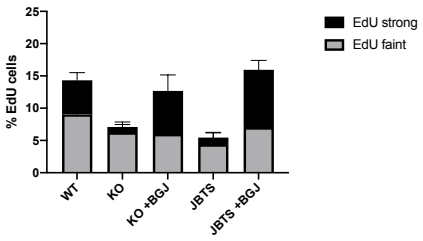

FIGURE 8. EdU pulse-chase experiment shows that neural progenitor proliferation is increased in *RPGRIP1L*-deficient organoids and can be rescued by blocking FGF signaling

(A) Immunofluorescence for SOX2 (in magenta) and EdU (in green) on cryosections from WT, *RPGRIP1L*-deficient (KO and JBTS patient) and *RPGRIP1L*-deficient +BGJ-398 organoids at day 18 – 2h after EdU pulse. **(B-C)** Graphs showing the % of EdU+ cells over the total number of nuclei stained with DAPI (B) and the % of EdU+/SOX2+ cells over the total number of SOX2+ cells (C) at day 18 – 2h after EdU pulse. Positive cells were counted in sections from different organoids per condition from one experiment (WT and *RPGRIP1L* KO: Wtc11=1; JBTS: NG2266 N=1). Each dot in the graph represents one organoid; mean ± SEM are shown. Asterisks denote statistical significance according to Ordinary-Way ANOVA after normal distribution testing (*P<0.033; ****P<0.0001) (B-C). **(D)** Immunofluorescence for SOX2 (in magenta), HUC/D (in blue) and EdU (in green) on cryosections from WT, *RPGRIP1L*-deficient (KO and JBTS patient) and *RPGRIP1L*-deficient +BGJ-398 organoids at day 23 – 5 days after the 2h EdU pulse (chase experiment). **(E-F)** Graphs showing the % of EdU-positive cells over the total number of nuclei stained with DAPI (E) and the % of EdU+/SOX2+ cells over the total number of SOX2+ cells at day 23 (chase experiment). Positive cells were counted in sections from different organoids per condition from one experiment (WT and *RPGRIP1L* KO: Wtc11=1; JBTS: NG2266 N=1). Each dot in the graph represents one organoid; mean ± SEM are shown. Asterisks denote statistical significance according to Ordinary-Way ANOVA after normal distribution testing (**P<0.0021; ****P<0.0001) **(G)** Graphs showing the ratio between “strong” and “faint” EdU labeling in the % of EdU+ cells over total nuclei. N: number of independent experimental replicates. Scale bars: 100 µm in A and D.

Supplementary 1

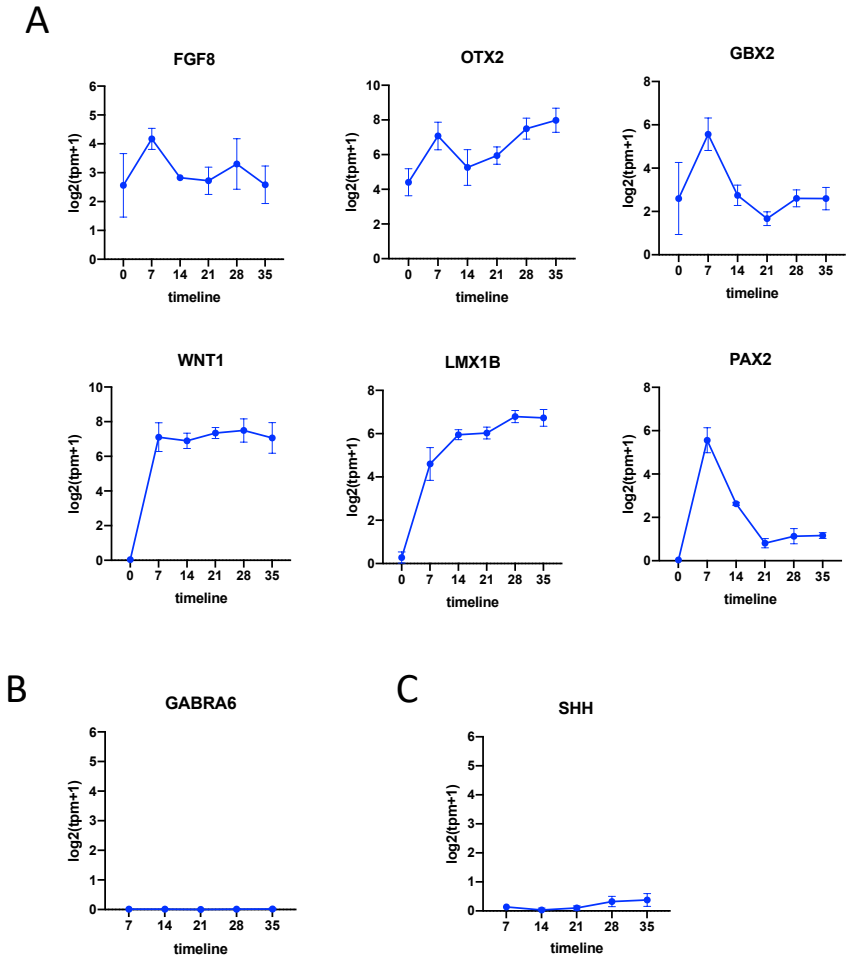

Supplementary Figure 1. MHB and other cerebellar markers expression in WT cerebellar organoids.

(A-C) Graphs based on the mean ± SEM of the Log2(tpm+1) values from the bulk RNASeq (N=4 independent experiments: N=3 Ph2 line, N=1 Wtc11 line; n>20 organoids per condition) showing the RNA expression levels of **(A)** MHB markers (*FGF8, OTX2, GBX2, WNT1, LMX1B, PAX2*), **(B)** GN marker (*GABRA6)*, and **(C)** *SHH*, in WT organoids along the differentiation protocol.

Supplementary 2

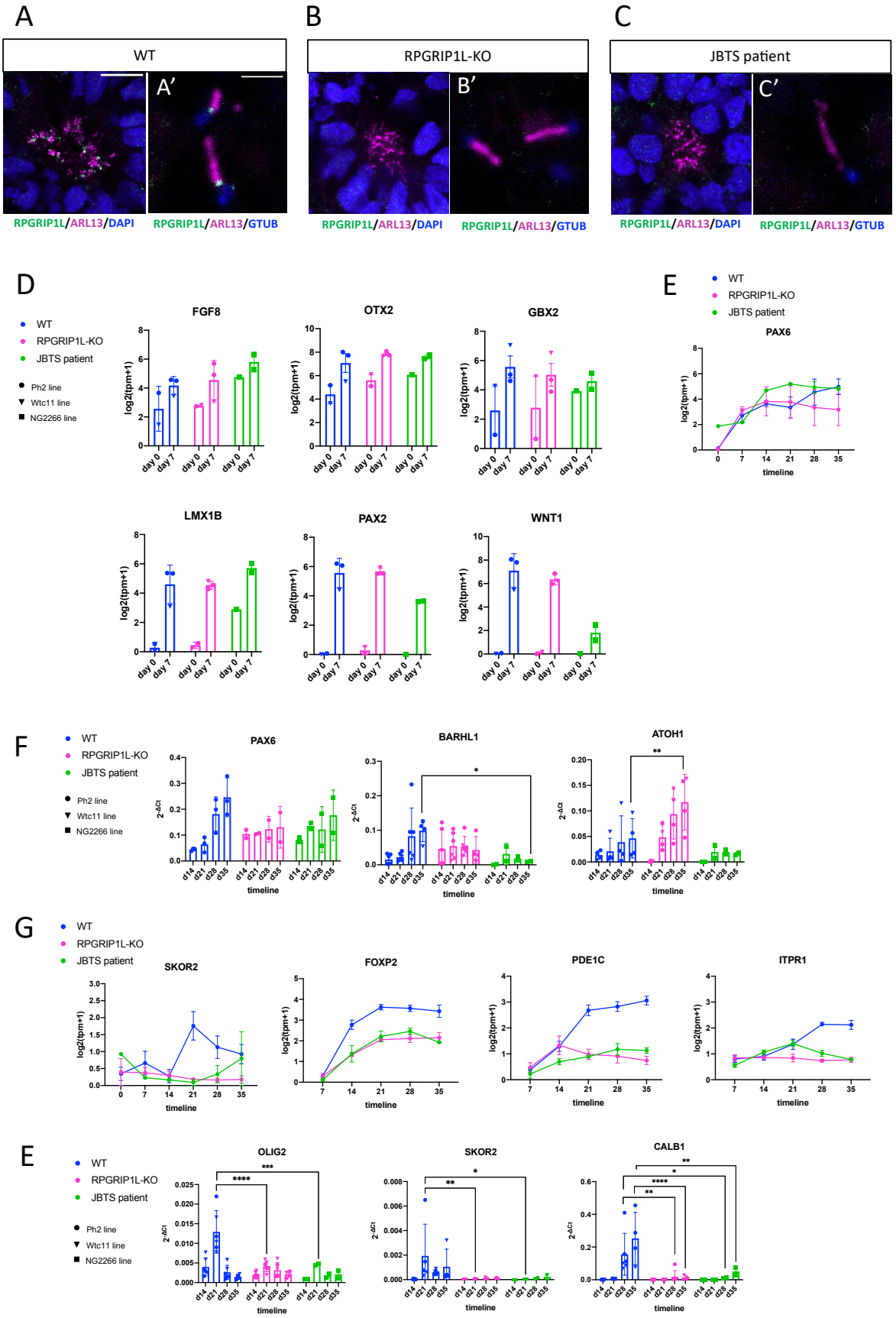

Supplementary Figure 2. Altered RNA expression of Purkinje Cell and Granule Cell Progenitor markers in *RPGRIP1L*-deficient cerebellar organoids

(A-C) Immunofluorescence for RPGRIP1L (in green), the ciliary marker ARL13B (in magenta) and the nuclear marker DAPI (blue, left panels) or the basal body marker GTUB (blue, A'-C') on cryosections from WT (A-A'), *RPGRIP1L* KO (B-B') and JBTS patient (C-C') organoids at day 21. Scale bars: 10 µm in A-C and 2 µm in A'-C'. **(D)** Graph showing temporal expression analysis of MHB markers (*FGF8, OTX2, GBX2, WNT1, LMX1B, PAX2*) in WT, *RPGRIP1L* KO and JBTS organoids at day 0 (WT and *RPGRIP1L* KO: Ph2 hiPSC N=1 – circular dots, Wtc11 hiPSCs N=1 – triangular dots; JBTS patient: NG2266 hiPSCs N=1 – squared dots) and day 7 (WT and *RPGRIP1L* KO: Ph2 hiPSC N=2 – circular dots, Wtc11 hiPSCs N=1 – triangular dots; JBTS patient: NG2266 hiPSCs N=2 – squared dots). Log2(tpm+1) values from bulk RNASeq analysis are displayed as mean ± SEM. **(E)** Graph showing temporal expression analysis of GCP marker *PAX6* over the differentiation protocol (WT and *RPGRIP1L* KO: Ph2 N=3, Wtc11 N=1; JBTS patient: NG2266 N=2). Log2(tpm+1) values from bulk RNASeq analysis are displayed as mean ± SEM. **(F)** qPCR analysis of GCP markers (*PAX6, BARHL1, ATOH1*) in cerebellar organoids at different timepoints from several independent experiments (each dot in the graph represents one independent experiment per timepoint and condition; circular dots represent Ph2 line, triangular dots represent Wtc11 line, squared dots represent NG2266 line). Mean ± SEM are indicated. Asterisks denote statistical significance according to ordinary Two-Way ANOVA (*P<0.033, **P < 0.0021). **(G)** Graph showing temporal expression analysis of PC markers (*SKOR2, FOXP2, PDE1C, ITPR1*) along the differentiation protocol (WT and *RPGRIP1L* KO: Ph2 N=3, Wtc11 N=1; JBTS patient: NG2266 N=2). Log2(tpm+1) values from bulk RNASeq analysis are displayed as mean ± SEM. **(H)** qPCR analysis of PC markers (*OLIG2, SKOR2, CALB1*) in cerebellar organoids at different timepoints from several independent experiments (each dot in the graph represents one independent experiment per timepoint and condition; circular dots represent Ph2 line, triangular dots represent Wtc11 line, squared dots represent NG2266 line). Mean ± SEM are indicated. Asterisks denote statistical significance according to ordinary Two-Way ANOVA (*P<0.033, **P < 0.0021, ***P<0.0002 and ****P< 0.0001). N: number of independent experimental replicates.

Supplementary 3

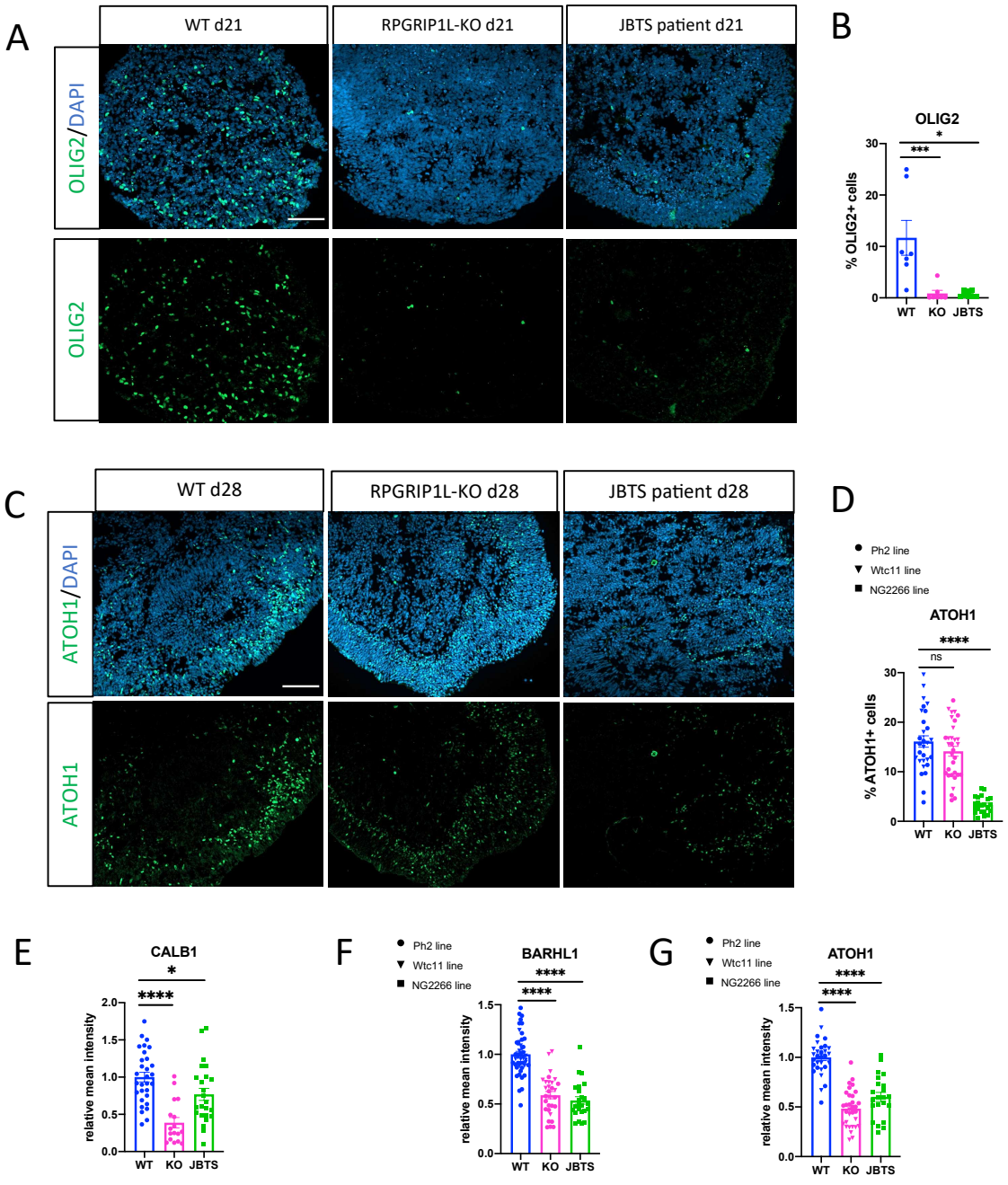

Supplementary Figure 3. *RPGRIP1L*-deficient cerebellar organoids present an altered number of cells expressing Purkinje cell and Granule cell progenitor markers

(A) Immunofluorescence for OLIG2 (PC progenitors) on cryosections from WT, *RPGRIP1L* KO and JBTS patient organoids at day 21. **(B)** Graph showing the % of OLIG2-positive cells over the total number of nuclei stained with DAPI. Each dot represents an organoid section. Several sections from different organoids were analyzed (WT: Ph2 N=1, *RPGRIP1L* KO: Ph2 N=1; JBTS patient: NG2266 N=1). Data are shown as mean ± SEM. Asterisks denote statistical significance according to One-Way ANOVA Kruskal-Wallis test with Dunn's correction (***P<0.0002 and ****P< 0.0001). **(C)** Immunofluorescence for ATOH1 (GCP) on cryosections from WT, *RPGRIP1L* KO and JBTS patient organoids at day 28. **(D)** Graph showing the % of ATOH1-positive cells over the total number of nuclei stained with DAPI. Positive cells were counted in more than 15 sections from different organoids per experiment per condition (WT: Ph2 N=2, Wtc11 N=1; *RPGRIP1L* KO: Ph2 N=2, Wtc11 N=1; JBTS patient: NG2266 N=2). Data are shown as mean ± SEM. Asterisks denote statistical significance according to One-Way ANOVA Kruskal-Wallis test with Dunn's correction (****P<0.0001). **(E-G)** Graphs showing the average intensity of CALB1 (E), BARHL1 (F), ATOH1 (G) labeling on cryosections from WT, RPGRIP1L KO and JBTS organoids at day 28. Each dot in the graph represents one independent experiment per condition; circular dots represent Ph2 line, triangular dots represent Wtc11 line, squared dots represent NG2266 line Relative mean intensity ± SEM is calculated considering the mean of WT levels as the reference value (1). Asterisks denote statistical significance according to One-Way ANOVA Kruskal-Wallis test with Dunn's correction (*P<0.033, and ****P<0.0001). N: number of independent experimental replicates. Scale bars: 100 µm in A and D.

Supplementary 4

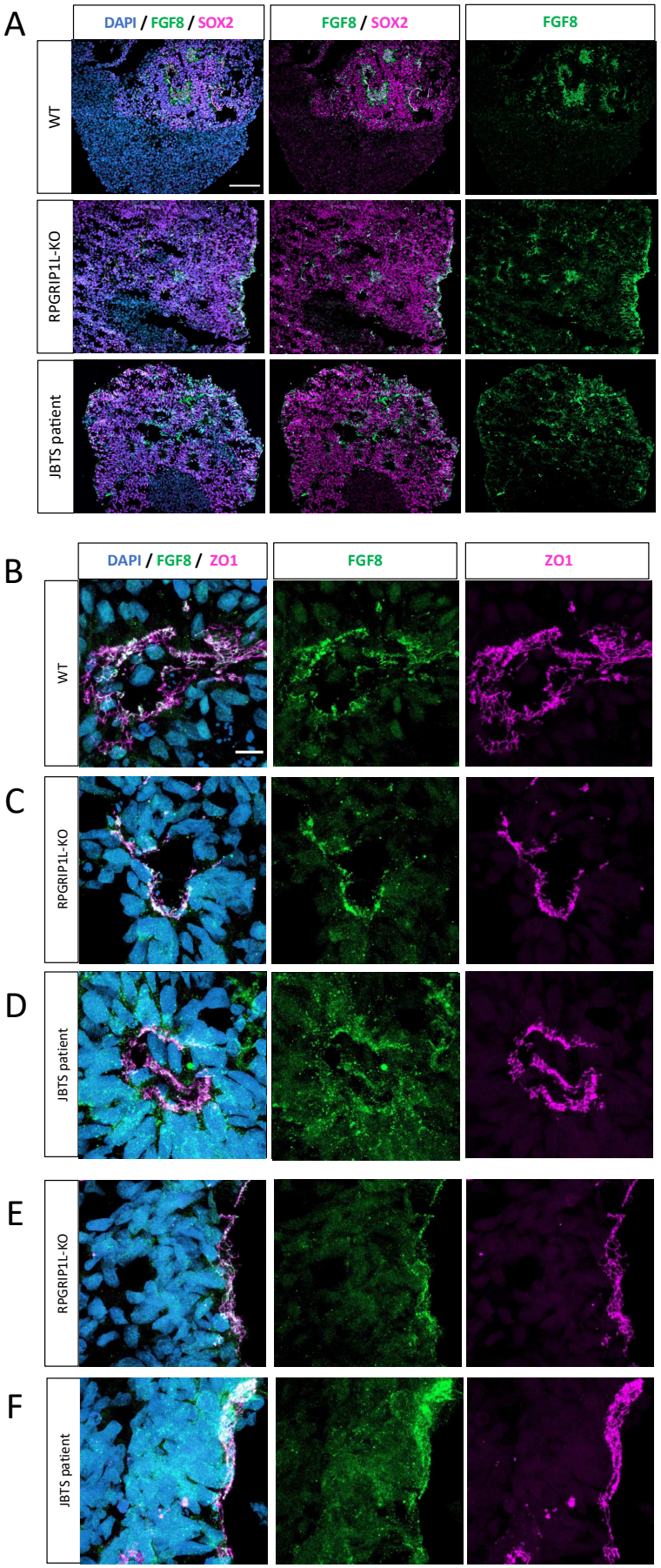

Supplementary Figure 4. FGF8 production by early apical progenitors and accumulation on apical sides

(A) Immunofluorescence for SOX2 (in magenta) and FGF8 (in green) on cryosections from day 14 WT, *RPGRIP1L* KO and JBTS patient organoids. Scale bar, 100 µm **(B-F)** Confocal images of FGF8 (green) and ZO1 (red) immunofluorescence showing accumulation of FGF8 protein at ZO1 apical sides of progenitor rosettes in WT (B), *RPGRIP1L* KO (C) and JBTS patient (D) organoids. *RPGRIP1L* KO (E) and JBTS patient (F) organoids also present FGF8 protein accumulation at ZO1 apical junctions at the organoid borders. Scale bars: 100 µm in A and 10 µm in B-F.

Supplementary 5

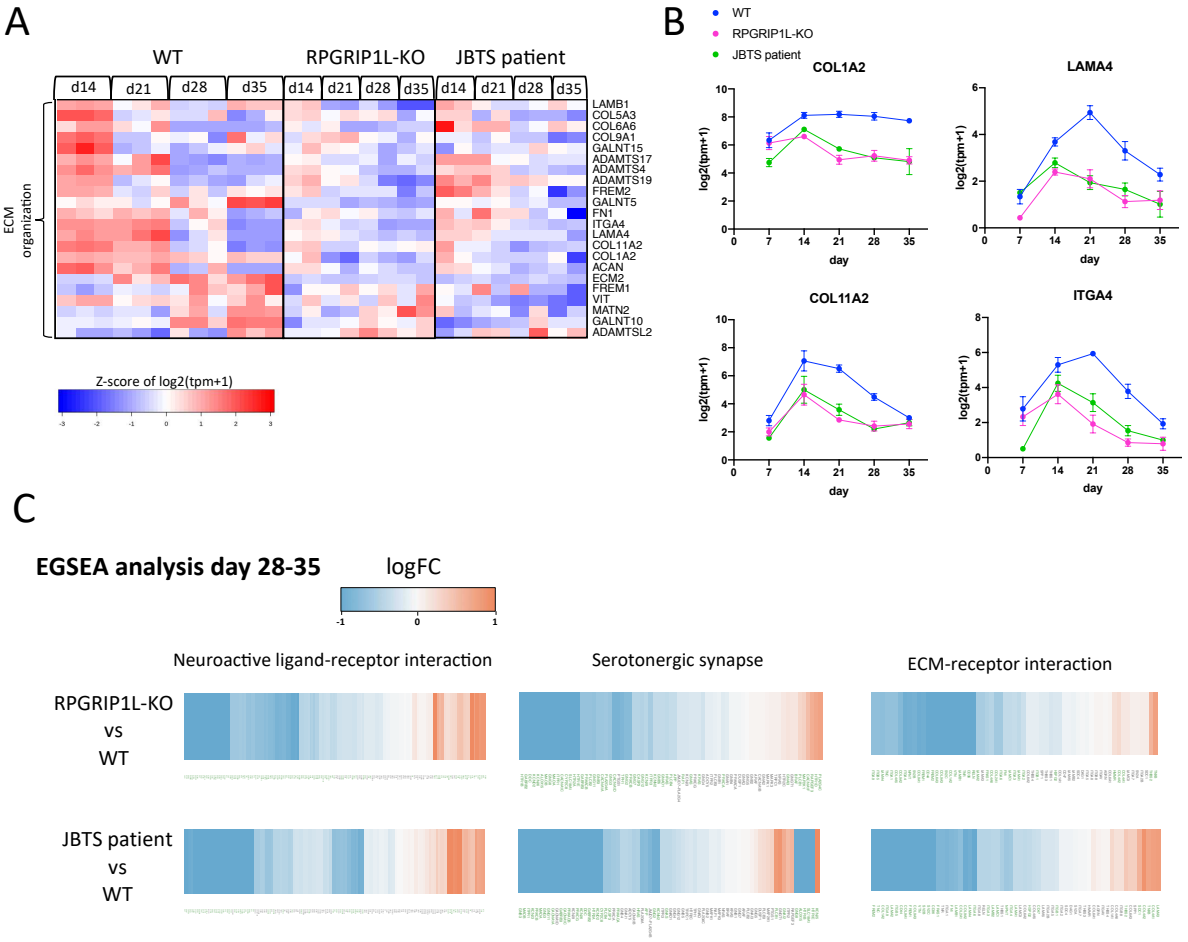

Supplementary Figure 5. Bulk RNAseq analysis revealed severe downregulation of genes involved in extracellular matrix components, ECM-receptor interactions and synapse formation and in RPGRIP1L-deficient organoids.

(A) Heatmap showing the z-score of the log 2(tpm+1) values of selected differentially expressed genes in WT and *RPGRIP1L*-deficient cerebellar organoids over time (WT Ph2 N=3; *RPGRIP1L* KO Ph2: N=2, JBTS patient: N=2). **(B)** Graphs showing temporal expression analysis of ECM related genes *COL1A2, LAMA4, COL11A2, ITGA4* in WT, *RPGRIP1L* KO, and JBTS patient cerebellar organoids along the differentiation protocol. Log2(tpm+1) values from bulk RNASeq analysis are plotted as mean ±SEM. (n>20 organoids per condition per experiment are collected; WT: Ph2 N=3, Wtc11 N=1; *RPGRIP1L* KO: Ph2 N=2, Wtc11 N=1; JBTS patient: NG2266 N=2). **(C)** EGSEA analysis performed on feature counts datasets from WT and *RPGRIP1L*-deficient organoids at day 28 of differentiation shows a prevalence of downregulated genes (blue) among the Neuroactive ligand-receptor interaction gene set, Serotonergic synapse gene set and ECM-receptor interaction gene set, in both *RPGRIP1L* KO and JBTS patient conditions. N: number of independent experimental replicates.

Supplementary 6

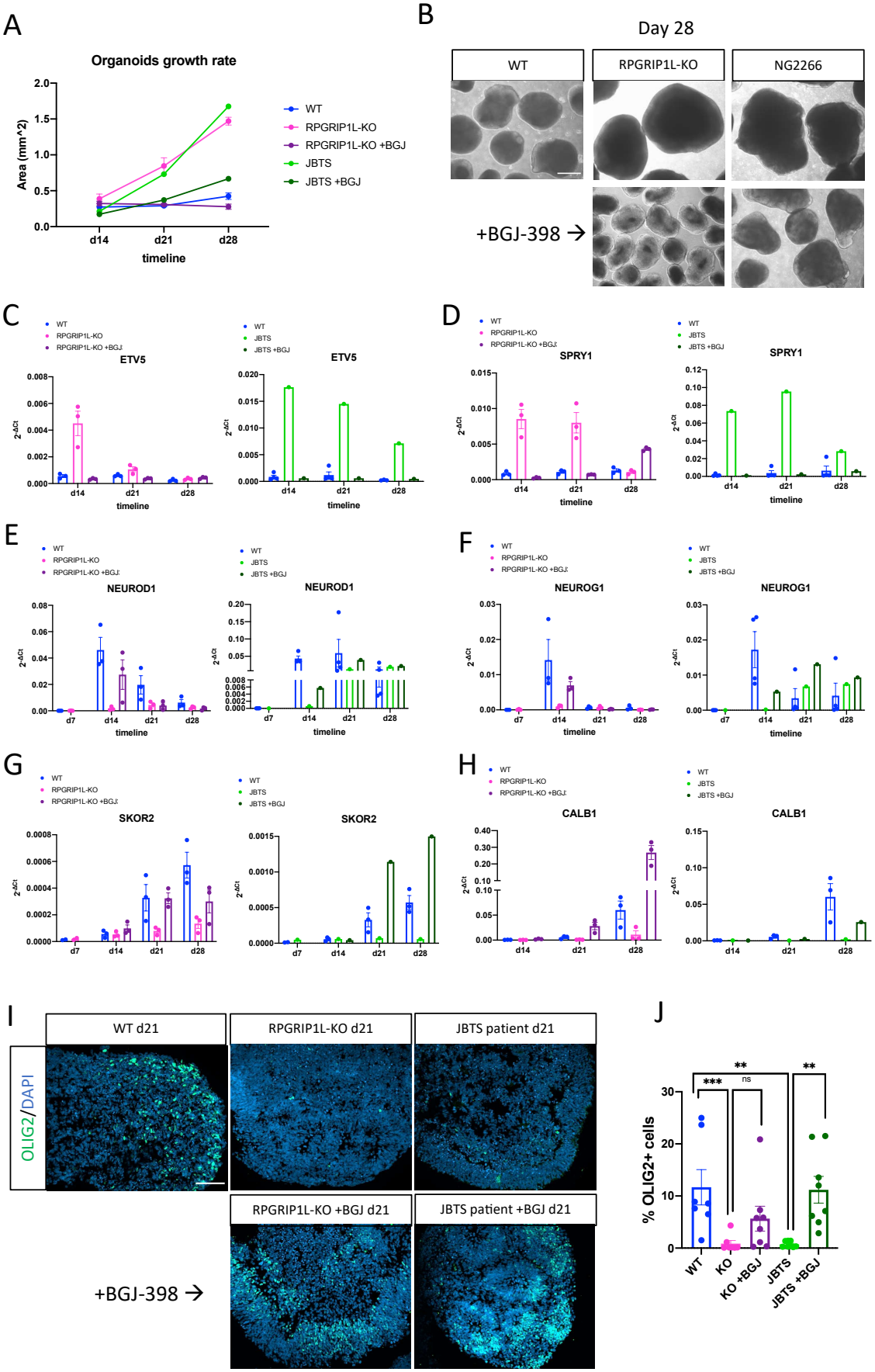

Supplementary Figure 6. FGF signaling inhibition rescues organoid size and gene expression in *RPGRIP1L* deficient organoids

(A) Graph representing the growth rate of cerebellar organoids. Organoid area was measured every 7 days from day 7 to day 35 of the differentiation protocol. Data are shown as the mean ± SEM of average organoid area from several independent experiments (WT and *RPGRIP1L* KO: N=3 Wtc11 line, JBTS patient: N=1 NG2266 line; n=10-60 organoids analyzed per experiment per condition). **(B)** Representative bright field images of cerebellar organoids at day 28. Scale bar, 500 µm. **(C-H)** Graphs showing gene expression levels (qPCR analysis) of *ETV5, SPRY1, NEUROD1, NEUROG1, SKOR2* and *CALB1* in WT, *RPGRIP1L*-deficient and *RPGRIP1L*-deficient +BGJ-398 cerebellar organoids at different timepoints (WT and *RPGRIP1L* KO: N=3 Wtc11 line; JBTS patient: N=1 NG2266 line). Data are shown as mean ± SEM. N: number of independent experimental replicates. **(I)** Immunofluorescence for OLIG2 (in green) on cryosections from WT, *RPGRIP1L*-deficient and *RPGRIP1L*-deficient +BGJ-398 organoids at day 21. Scale bar, 100 µm. **(J)** Graphs showing the % of OLIG2^{+} cells over the total number of nuclei stained with DAPI. Each dot in the graph represents one organoid section; mean ± SEM are shown (N=1). Asterisks denote statistical significance according to One-Way ANOVA Kruskal-Wallis test with Dunn's correction (**P<0.0021; ****P<0.0001). N: number of independent experimental replicates.

Supplementary 7

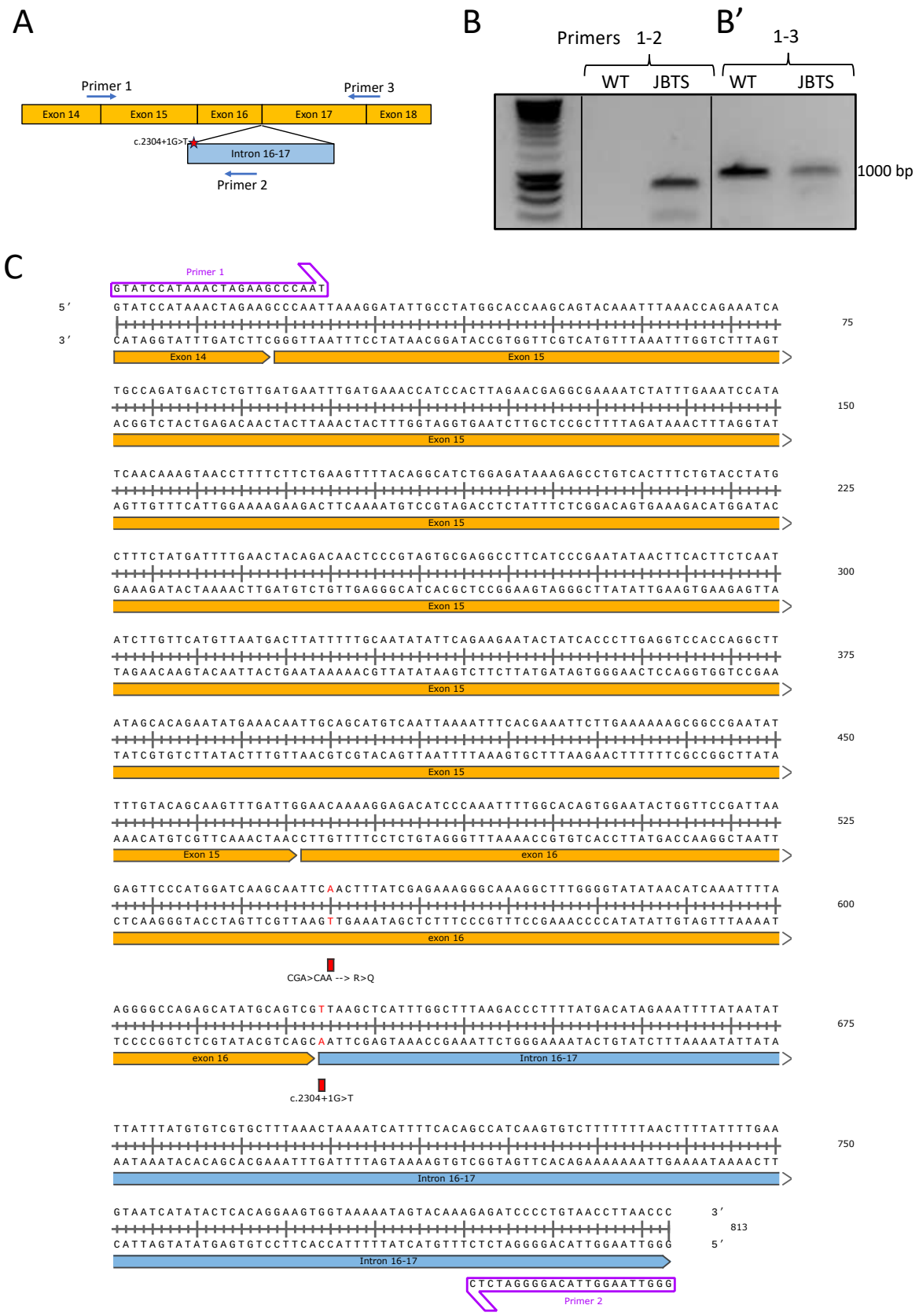

Supplementary Figure 7. NG2266 splice variant c.2304+1G>T results in intron retention.

(A) Schematic representation of *RPGRIP1L* gene exons 14-18 and PCR primers position to analyze cDNA products of *RPGRIP1L* gene in JBTS patient cells (NG2266 line) compared to WT (Ph2 line). **(B)** PCR~~s~~ products from JBTS patient and WT cerebellar cDNAs, templated by primer pairs as indicated, were analyzed by agarose gel electrophoresis and visualized with ethidium bromide. The primer pair 1-2 only amplifies JBTS patient cDNA, showing intron 16-17 retention. The primer pair 1-3 amplify both the second JBTS patient allele (encoding the *RPGRIP1L* Q684X variant) and WT cDNA. **(C)** Sequence of the PCR product templated by primer pair 1-2 on cDNA derived from NG2266 cell line.

Table S1.

primary Antibody	host	company	reference
Atoh1(Math1)	rabbit	Cohesion Biosciences	CQA1401
Barhl1	rabbit	Atlas	HPA004809
Calbindin	rabbit	Swant	CB-38
Fgf8	mouse IgG1	ReD system	MAB323
HuC/HuD (16A11) Elav	mouse IgG2b	Molecular Probes	A-21271
Inpp5e	rabbit	Proteintech	17797-1-AP
NeuroD1	mouse IgG1	Proteintech	66691-1-Ig
Olig2	rabbit	Millipore	AB9610
Sox2	rabbit	Millipore	AB5603
Zo1	rabbit	Life technologie	617300
γ-Tubulin	mouse IgG1	Sigma	T6557

Table S2.

secondary Antibody	host	conjugate	company
Mouse IgG1	goat	Alexa488	Molecular Probes
Mouse IgG1	goat	Alexa633	Molecular Probes
Mouse IgG2b	goat	Alexa568	Molecular Probes
Rabbit	goat	Alexa488	Molecular Probes
Rabbit	goat	Alexa568	Molecular Probes
Rabbit	goat	Alexa633	Molecular Probes

Table S3.

Gene	Forward	Reverse
ATOH1	GTTATCCCGTCGTTCAACAACG	TGGGCGTTTGTAGCAGCTC
BARHL1	CGCGGAGGACTTTAGAGACAA	AGCTGGAGATCTCGCGGTC

CALB1	GGAAGTGGTTACCTGGAAGGA	CTCTTTGCCCATACTGATCCAC
ETV4	GTGGTGATCAAACAGGAACAGAC	TGTGTGGAGGTACATTGATGCG
ETV5	TGTTGTGCCTGAGAGACTGGA	GGTCATCAAGAAGGGTGACCA
FGF8	GACCCCTTCGCAAAGCTCAT	CCGTTGCTCTTGGCGATCA
GAPDH	CAACGGATTTGGTCGTATTGG	GCAACAATATCCACTTTACCAGAGTTA
NEUROD1	ATCATGAGCGAGTCATGAGTGC	GCACAGTGGGTTCGTTTCCC
NEUROG1	CCCTAGTCAGCAGGCAATAGAT	TCAGGTATCCCCGACTGCTTTA
OLIG2		
PAX6	TGCGACATTTCCCGAATTCTGC	CAGTCTCGTAATACCTGCCCA
SKOR2	ACACGCCTAAAGACACCCAG	ACGCCAGCAGGATGTCGTT
SPRY1	CTTTGCATTAGGCATTTCGGCC	ATTCCGCACGTTGGGCAAGT
SPRY4	CTCCTCAAAGGCCCCTAGAA	GGCTGGACCATGACTGAGTT